Computational investigation of single and multi-jet array impingement boiling

Computational investigation of single and multi-jet array impingement boiling

D. Wright [a], K. J. Craig [a,*], P. Valluri [b], J. P. Meyer [a]

[a] Department of Mechanical and Aeronautical Engineering, University of Pretoria, Pretoria, South Africa
[b] Institute for Multiscale Thermofluids, School of Engineering, The University of Edinburgh, Edinburgh, United Kingdom

Abstract

Jet impingement boiling has been studied extensively and has been identified as one of the most promising thermal management techniques for high heat flux applications. Unfortunately, only a few numerical studies have been reported in literature and they are mostly limited to single jets. In the present study, both submerged single round jets and confined multi-jet arrays are investigated numerically, using the Eulerian multiphase framework with the Rensselaer Polytechnic Institute (RPI) boiling model to predict heat transfer. The numerical results of the single jet case correlate well with reported experimental data and previously reported numerical results. The numerical results of the multi-jet array correlate well with experimental data reported in the literature, proving that the RPI boiling model can successfully predict the heat transfer of jet array boiling. The effect of conjugate heat transfer in jet impingement boiling heat transfer is also investigated for both single and multiple jet cases. The single-jet results agree with previous reported numerical studies. To improve numerical convergence, especially for higher heat fluxes, use was made of a hydrostatic pressure gradient at the outlet. This allowed for significant improvement in the convergence of the continuity equation. Finally, parametric analyses were conducted for both single and multi-jet arrays in the fully developed nucleate boiling regimes. Parameters included jet-to-surface spacing, Reynolds number and subcooling. The results for the single jet correlates well with the observations of experiments reported in the literature. The results for the multi-jet array showed less sensitivity to changes in jet velocity at low jet-to-surface spacing than the single jet case. Both single and multi-jet cases showed that reducing the subcooling resulted in an onset of nucleate boiling at lower heat fluxes and that the boiling curve shifted to the left in the nucleate boiling regime.

Nomenclature

A	area [m^2]	Greek Symbols	
A_b	area of influence	α	phase volume fraction
A_i	interfacial area concentration	ε	dissipation rate
A_w	interfacial area density of the wall	λ	liquid phase diffusivity
C	correlation constant	μ	dynamic viscosity [$N{\cdot}s/m^2$]
C_p	constant pressure specific heat capacity [$J/kg{\cdot}K$]	ρ	density [kg/m^3]
C_{vm}	virtual mass coefficient	σ	surface tension [N/m]
D	diameter [m]	Subscripts	
F	force [N]	C	liquid phase convection
g	gravitational acceleration [m/s^2]	E	evaporation
G	turbulence production rate [$kg/m{\cdot}s^3$]	G	gas
h	convection heat transfer coefficient [$W/m^2{\cdot}K$]	L	liquid

* Corresponding author. Tel: +27 83 310 8946; E-mail address: ken.craig@up.ac.za

h_{fg}	latent heat of vaporization [J/kg]	L_s	liquid side of the interfacial area
H	Jet height [m]	L_v	interaction between liquid and vapour phases
H/D	jet-to-surface spacing	m	mixture
Ja	Jacob number	N	jet nozzle exit
k	turbulent kinetic energy [m^2/s^2]	p	phase p
$\dot{m}$	mass transfer rate [kg/s]	pq	interaction between phases p and q
N	number of jets	q	phase q
p	pressure [Pa]	Q	quenching
Pr	Prandtl number	S	surface
q''	heat flux [W/m^2]	sat	saturation
Q	interfacial heat transfer [W/m^3]	sub	subcooling
Re	Reynolds number	V	vapour
S	source term in energy equation [W/m^3]	vs	vapour side of the interfacial area
t	periodic time [s]	w, W	wall
T	Temperature [K]	Acronyms	
ΔT_{sat}	surface superheat [K]	CHF	Critical Heat Flux
ΔT_{sub}	surface liquid subcooling [K]	HTC	Heat Transfer Coefficient
u, U	velocity [m/s]	ONB	Onset of Nucleate Boiling
		$ONBD$	Onset of Nucleate Boiling Departure

1 Introduction

Conventional cooling methods based on single-phase convection are inadequate for the heat dissipation demands of high-performance electronic devices. Phase-change cooling methods which in addition to sensible heat e.g. [1], utilise the latent heat of the cooling fluid offer promise to extract large amounts of heat at relatively low device surface temperatures. Research into cooling high-power electronic devices using flow boiling in microchannel heat sinks has been performed by many researchers, e.g. [2] and [3].

Jet impingement as a heat transfer enhancement mechanism has been used in various engineering devices, e.g., for internal cooling of turbine blades [4], and using various configurations and fluids, e.g., annular jets [5] or multiple air slots [6]. The enhancement typically occurs close to the impingement location with further enhancement possible due to transition of the laminar wall jet close to the stagnation point to turbulent flow.

The comprehensive literature review of two-phase cooling solutions by Mudawar [7] suggests that jet impingement boiling is one of the most promising two-phase thermal management solutions for very high heat flux applications and has received considerable attention in the literature. There are a large number of adjustable geometric and hydrostatic parameters in jet impingement thermal management devices, thereby giving ample opportunities to tailor designs for high levels of heat dissipation or for large surface areas in low pressure drop applications [8]. Jet impingement in the nucleate boiling regime can achieve high rates of heat transfer for only a modest increase in wall superheat, making it an attractive option for thermal management devices [9].

Fundamental investigations of jet impingement boiling were first reported in the literature in 1970, when Copeland [10] experimentally investigated a water jet impinging on a heated nickel-plated copper block. In 1973, Katto and Kunihiro [11] experimentally investigated the burn-out characteristics of a pool boiling system by using both mechanical means and a submerged liquid jet impinging on the heated surface to reduce the vapour mass. It was shown that the addition of an impinging jet resulted in a completely different burn-out mechanism than pool boiling as well as a higher burn-out heat flux,

which increases with jet velocity. However, the jet velocity had little influence on the average heat transfer of submerged jet impingement in the fully developed nucleate boiling regime.

Similarly, Struble and Witte [12], while studying heat flux measurement techniques for R113 boiling jets observed that heat transfer in the fully developed nucleate boiling regime increased only a little with jet velocity and subcooling. Zhou and Ma [13] investigated the heat transfer of submerged round jet impinging on simulated microelectronic chips using R113 as the heat transfer fluid. They found that varying jet velocities from 0 to 11.355 m/s has a negligible influence on heat transfer in fully developed nucleate boiling regime. However, heat transfer in the nucleate boiling regime increased with liquid subcooling.

Cardenas and Narayanan [14] investigated the heat transfer characteristics of submerged round impinging jets in the saturated nucleate boiling regime using FC-72 as the heat transfer fluid. They found that the incipient boiling wall superheat is not a function of the jet Reynolds number and jet diameter. They concluded that jet kinetic energy is key towards critical heat flux (CHF) enhancement noting that it increases with jet velocity. Zhao et al. [15] investigated confined water jet heat transfer from porous surfaces finding that CHF increases with jet Reynolds number and subcooling but that heat transfer in the fully developed nucleate boiling regime is not a function of jet Reynolds number and liquid subcooling. Hong et al. [16] whilst investigating confined subcooled jet array boiling using an aqueous ethylene glycol solution found that the liquid subcooling and jet-to-jet spacing play a significant role and that there exists an optimal jet-to-jet spacing for a fixed flow rate. There also exists an optimal jet-to-surface spacing to achieve the highest CHF. Clark et al. [17] identified nucleate boiling as the dominant heat transfer mechanism for confined jet impingement.

CHF increases with jet velocity in free-surface jets, submerged jets, as well as confined jets [17]. Cardenas and Narayanan [18] also showed that the degree of subcooling has little effect on the boiling curve in the fully developed nucleate boiling regime. However, similar to observations made by Zhao et al. [15], they noted that higher degrees of subcooling could extend the fully developed nucleate boiling regime and thus increase the CHF. Li et al. found that the nucleate boiling heat transfer coefficient in the fully developed regime is unaffected by subcooling, however, the wall superheat at the onset of nucleate boiling (ONB) increases with subcooling [19].

Cui et al. [20] observed that crossflow in multi-jet arrays has a significant influence on the boiling curve for both smooth and pin-fin surfaces. Hong et al. found that for a constant total mass flowrate, increasing the number of jets improves overall heat transfer [16].

Only a few numerical investigations are described in the literature. Narumanchi et al. [21] reported the first numerical investigation of jet impingement boiling, when they successfully predicted the heat transfer of the single water jet experiment by Katto and Kunihiro [11], using the Rensselaer Polytechnic Institute (RPI) boiling model implemented in the computational fluid dynamics (CFD) code Fluent. Studying a single jet, Abishek et al. [22] investigated the effect of heater size and Reynolds number on the heat flux partitioning of the RPI boiling model in subcooled jet impingement boiling. They found that the liquid phase convective heat flux component increases with jet velocity while the quenching and evaporative heat flux components were nearly unaffected. They also found that for any specified heat flux, the surface temperature reduces with the heater surface size, implying higher effectiveness of jet impingement boiling for localised heat sources. For the same geometry used by Narumanchi [21], Qiu et al. [23] performed a new validation study and investigated the influence of conjugate heat transfer in the copper heating block, they found that the effects of conjugate heat transfer must be considered should the experimental setup have a copper block of significant mass. Esmailpour et al. [24] conducted a numerical parametric study for a subcooled single water jet showing that heat transfer decreases with increasing jet-to-surface spacing for $2 \leq H/D \leq 6$ but increases with jet velocity for $2500 \leq Re \leq 10000$.

Previous numerical investigations already proved that the RPI boiling model can predict jet impingement boiling heat transfer with acceptable accuracy. However, most numerical studies to date are limited to single jets and only cover lower heat fluxes of the nucleate boiling regime. The objective of the current study is to validate a single jet and multi-jet array, confirm the effect of conjugation for

both, and perform a parametric analysis using jet-to-surface spacing and Reynolds number as parameters. We also present computational enhancements in order to predict the boiling curves much closer to the CHF.

The numerical framework is discussed in Section 2. Section 3 presents validation against existing experimental models for single jet and multi-jet cases. A parametric study is presented in section 4 along with an in-depth discussion of the results. Section 5 presents the key conclusions drawn.

2 Problem Definitions and Numerical Modelling Methodology

In this Section, we describe the problems of 2D axisymmetric jet simulating experiments of Katto and Kunihiro [11] and 3D jet array simulating experiments of Devahdhanush and Mudawar [25]. We also present the modelling and numerical methodology used.

2.1 2D Axisymmetric single jet

The experimental study by Katto and Kunihiro [11] considered a single submerged round water jet impinging on a conical heated copper block with an upper surface diameter of 10 mm. The jet had a nozzle exit velocity of 2 m/s and inlet subcooling of 3 °C at atmospheric pressure, translating to an inlet temperature of 97 °C. The nozzle had an exit diameter of 1.6 mm with a jet-to-surface spacing of 3 mm, submerged 2 mm below the free surface. It must be noted that two numerical investigations have been conducted of this experimental setup: Narumanchi et al. [21] and Qiu et al. [23]. The former neglected the effects of conjugation heat transfer, where the latter considered the effects of it. In this study, both cases are considered. Since only one round jet impinges on a conical heated block, the domain is axisymmetric. The 2D axisymmetric computational domains of the case without conjugation and the case with conjugation are illustrated in Fig. 1 and Fig. 2, respectively.

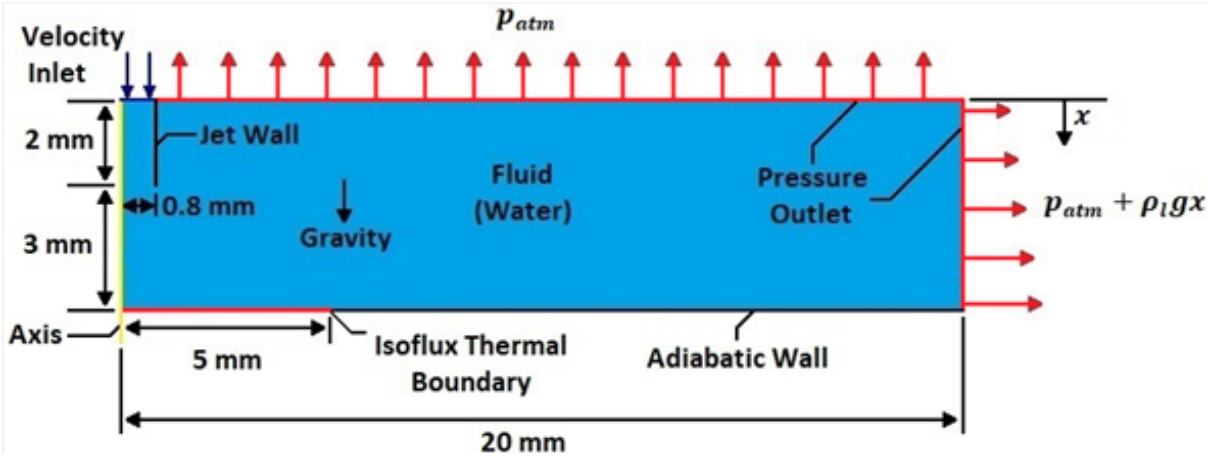

Fig. 1. 2D Axisymmetric domain based on Katto and Kunihiro experiment [11] without considering conjugation heat transfer effects [23]. Hydrostatic pressure gradient included at radial outlet.

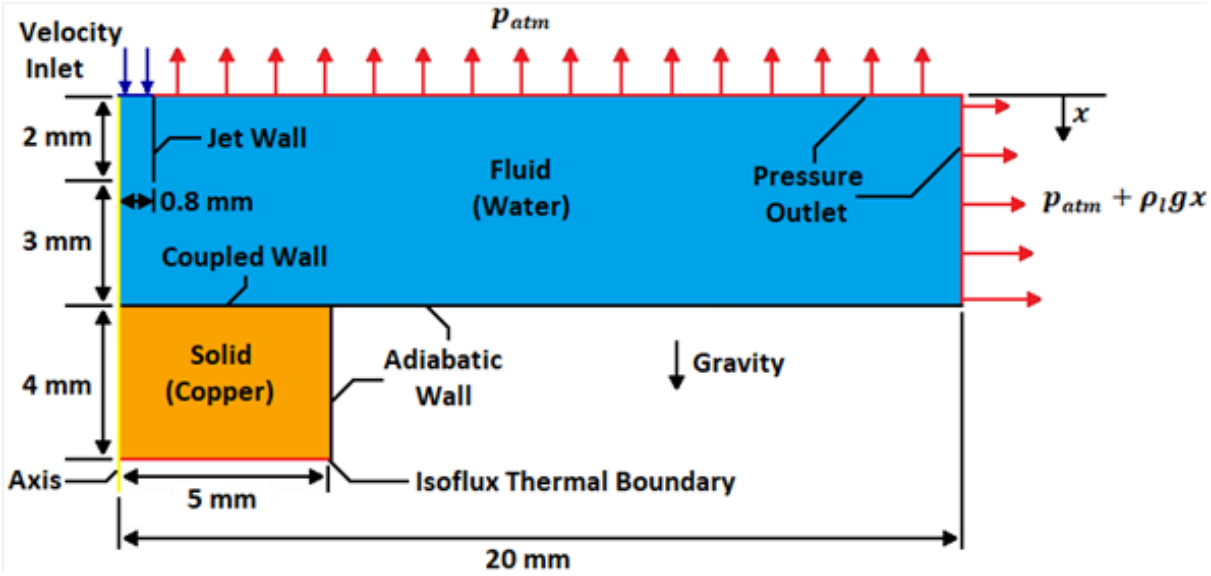

Fig. 2. 2D Axisymmetric domain based on Katto and Kunihiro experiment [11] considering conjugation heat transfer effects [23]. Hydrostatic pressure gradient included at radial outlet.

2.2 3D Jet Array

We consider the experimental study by Devahdhanush and Mudawar [25] employing boiling round jets, configured in confined arrays impinging on square surfaces. Devahdhanush and Mudawar [25] investigated influence of several parameters on the CHF with R134a as the working fluid. Here we simulate one of their cases for which the boiling curve was documented. As in Section 2.1, this experiment investigates the effects of conjugation heat transfer. Since the jet array consists of multiple round jets impinging on a square target, it is important to note the domain is not axisymmetric and requires a 3D mesh. The computational requirements can be reduced significantly by only modelling a quarter of the domain with symmetry planes. The computational domains are illustrated in Fig. 3 and Fig. 4, for the two cases, respectively. It should be noted that the single water jet has a pressure outlet boundary at the top while the multi-jet array is confined by a wall. In the case of the single water jet, the pressure boundary allows reversed flow, introducing additional subcooled liquid into the domain while in the case of the multi-jet array, the confinement wall prevents reversed flow. This could influence the difference in results between the two cases, as the degree of subcooling in the domains is influenced by the amount of reversed flow at the pressure outlets.

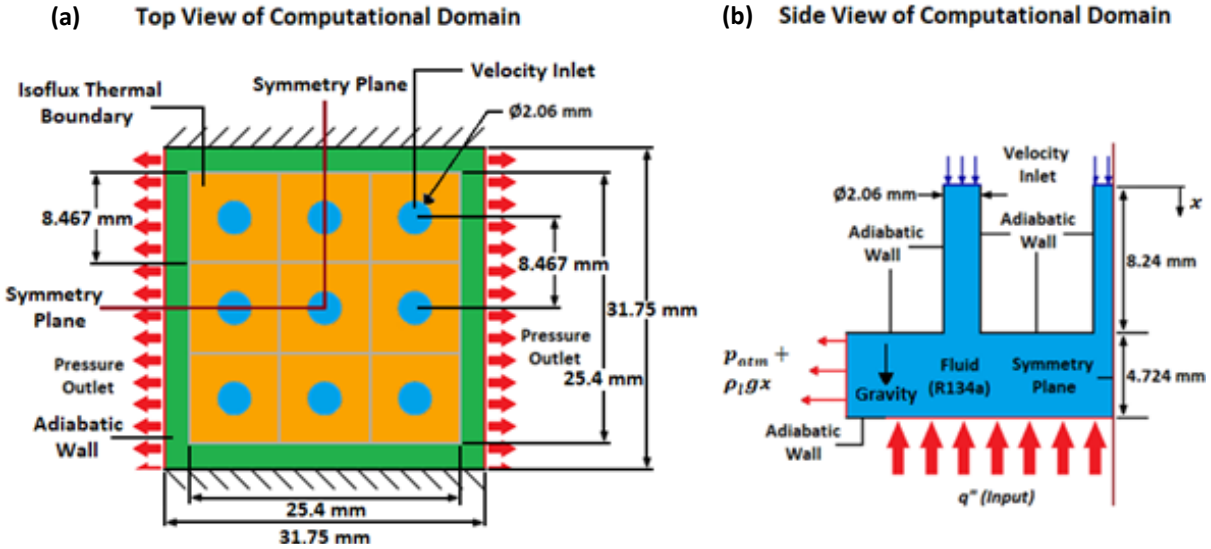

Fig. 3. 3D Quarter symmetry domain adapted from the experiments of Devahdhanush and Mudawar [25] without considering conjugation (no solid modelled), top view (a) and side view (b).

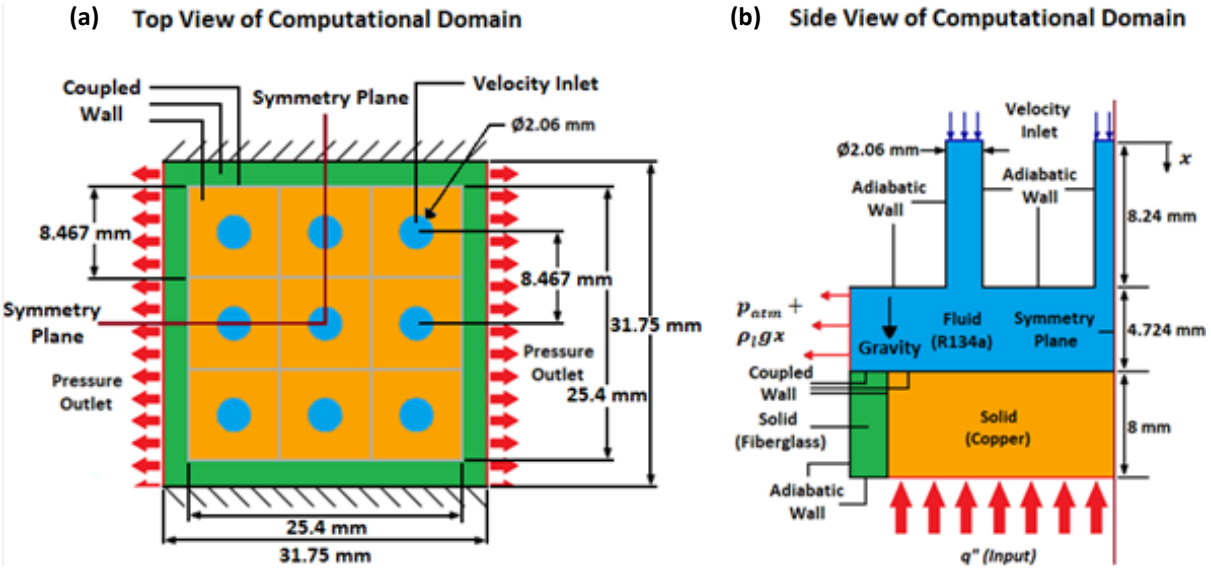

Fig. 4. 3D Quarter symmetry domain adapted from the experiments of Devahdhanush and Mudawar [25] considering conjugation heat transfer effects (with solid copper and fiberglass insulation), top view (a) and side view (b).

2.3 Modelling

In the current study, subcooled nucleate boiling is modelled with the commercial CFD software suite ANSYS Fluent 2021R1. The Eulerian multiphase model is used as the simulation framework with liquid as the primary phase and vapour as the dispersed phase. The RPI wall boiling model is implemented with the Eulerian multiphase model to predict the heat transfer of subcooled boiling. The mathematical descriptions of the numerical models used in ANSYS Fluent are presented in this section as adapted from [26]. All numerical models presented in this section were already implemented in ANSYS Fluent, thus no user defined functions were used.

The Eulerian multiphase model treats the phases in a multiphase mixture as interpenetrating continua, where, the volume of one phase cannot be occupied by another phase. The volume of the multiphase mixture thus consists of a portion of each phase of which the volumetric contribution is denoted by a volume fraction, α. The sum of the volume fractions of all phases must be one in each control volume. The conservation of mass, momentum and energy equations are solved for each phase separately. The conservation equations are coupled with pressure and interphase exchange coefficients, which are dependent on the mixture type.

2.3.1 Governing equations

The conservation of mass for phase *q* is:

$$\frac{\partial}{\partial t}\left(\alpha_q \rho_q\right) + \nabla \cdot \left(\alpha_q \rho_q \vec{u}_q\right) = \sum_{p=1}^{n}\left(\dot{m}_{pq}\right) \tag{1}$$

with, α_q the volume fraction of phase *q*, ρ_q the density of phase *q*, $\vec{u}_q$ the velocity of phase *q*, $\dot{m}_{pq}$ the interphase mass transfer rate between phases *p* and *q*, and *n* the number of phases.

The momentum conservation equation for phase *q* is:

$$\begin{aligned}&\frac{\partial}{\partial t}\left(\alpha_q \rho_q \vec{u}_q\right) + \nabla \cdot \left(\alpha_q \rho_q \vec{u}_q \vec{u}_q\right) \\ &= -\alpha_q \nabla \mathrm{p} + \nabla \cdot \bar{\bar{\tau}}_q + \alpha_q \rho_q \vec{g} + \sum_{p=1}^{n}\left(\vec{R}_{pq} + \dot{m}_{pq}\vec{u}_{pq}\right) + \left(\vec{F}_q + \vec{F}_{lift,q} + \vec{F}_{wl,q} + \vec{F}_{vm,q} + \vec{F}_{td,q}\right)\end{aligned} \tag{2}$$

where, $\bar{\bar{\tau}}_q$ is the stress tensor, $\vec{R}_{pq}$ the interfacial drag force between phases *p* and *q*, $\vec{u}_{pq}$ the interphase velocity, $\vec{g}$ the gravitational acceleration vector, p the pressure, $\vec{F}_q$ an external body force, $\vec{F}_{lift,q}$ the lift force, $\vec{F}_{wl,q}$ the wall lubrication force, $\vec{F}_{vm,q}$ the virtual mass force, and $\vec{F}_{td,q}$ the turbulent dispersion force.

The energy conservation equation for phase *q* is:

$$\frac{\partial}{\partial t}\left(\alpha_q \rho_q h_q\right) + \nabla \cdot \left(\alpha_q \rho_q \vec{u}_q h_q\right) = \alpha_q \frac{dp_q}{dt} + \bar{\bar{\tau}}_q : \nabla \vec{u}_q - \nabla \cdot \vec{q}_q + S_q + \sum_{p=1}^{n}\left(Q_{pq} + \dot{m}_{pq} h_{pq}\right) \tag{3}$$

where, h_q is the specific enthalpy of phase *q*, $\vec{q}_q$ the heat flux, Q_{pq} the energy exchange term between phases *p* and *q*, S_q the source term, and h_{pq} the difference in the specific enthalpies of phases *p* and *q*.

2.3.2 Turbulence modelling

The mixture *RNG k-ε* model is used in the current work to model the turbulence of the multiphase mixture. It accounts for dispersed phase induced turbulence by adding additional source terms in the turbulent kinetic energy and dissipation equations. The turbulent kinetic energy equation for the mixture is as follows:

$$\frac{\partial}{\partial t}\left(\rho_m k\right) + \nabla \cdot \left(\rho_m \vec{u}_m k\right) = -\nabla \cdot \left(\alpha_{k,m} \mu_{t,m} \nabla k\right) + G_{k,m} - \rho_m \varepsilon + S_{k,m} \tag{4}$$

where, ρ_m is the mixture density, *k* the turbulent kinetic energy, $\vec{v}_m$ the mixture velocity, *ε* the dissipation rate, $\alpha_{k,m}$ the inverse effective Prandtl number for *k*, $\mu_{t,m}$ the mixture viscosity, $G_{k,m}$ the turbulence production rate, and $S_{k,m}$ the dispersed phase-induced turbulence production source term.

The dissipation rate equation for the mixture is as follows:

$$\frac{\partial}{\partial t}\left(\rho_m \varepsilon\right) + \nabla \cdot \left(\rho_m \vec{u}_m \varepsilon\right) = -\nabla \cdot \left(\alpha_{\varepsilon,m} \mu_{t,m} \nabla \varepsilon\right) + \frac{\varepsilon}{k}\left(C_1 G_{k,m} - C_2 \rho_m \varepsilon\right) - R_\varepsilon + S_{\varepsilon,m} \tag{5}$$

where, $\alpha_{\varepsilon,m}$ is the inverse effective Prandtl number for *ε*, C_1 and C_2 are model constants, R_ε the RNG additional term, and $S_{\varepsilon,m}$ the dispersed phase-induced dissipation rate source term.

2.3.3 Interphase transfer models

The interfacial area concentration between phases is an important parameter for determining heat, mass, and momentum transfer through the interface between phases. The interfacial area concentration is modelled with the Ishii interfacial area model [26] and is given by the following correlation:

$$A_i = \frac{6\left(1-\alpha_p\right) min\left(\alpha_p, \alpha_{p,crit}\right)}{d_p\left(1 - min\left(\alpha_p, \alpha_{p,crit}\right)\right)} \tag{6}$$

with, $\alpha_{p,crit} = 0.25$.

The liquid-vapour mass transfer rate in Eq. (1), is determined based on the evaporation and condensation model, and is formulated as follows [26]:

$$\sum_{p=1}^{n}\left(\dot{m}_{pq}\right) = \dot{m}_{lv} = \frac{[h_{ls}(T_l - T_{sat}) + h_{vs}(T_v - T_{sat})]A_i}{h_{fg}} + \frac{q_E^{"} A_w}{h_{fg} + Cp_l(T_{sat} - T_l)} \tag{7}$$

where, h_{fg} is the latent heat of vaporization, Cp_l is the specific heat capacity of the liquid phase, *T* the temperature with subscripts *l*, *sat* and *v* referring to the liquid phase, saturation state, and vapour phase, respectively. A_w is the interfacial area density of the wall, and $q_E^{"}$ is the evaporative heat flux component of the RPI boiling model. Also, h_{ls} and h_{vs} are the liquid and vapour side heat transfer coefficients, respectively calculated according to the Ranz-Marshall correlation[27] for the 2D axisymmetric jet:

$$Nu_p = 2.0 + 0.6\sqrt{Re_p}Pr^{\frac{1}{3}} \tag{8}$$

We employ the Tomiyama correlation [28] for the 3D jet array, as it is more applicable for lower Reynolds numbers

$$Nu_p = 2.0 + 0.15Re_p^{0.8}Pr^{0.5} \tag{9}$$

The interfacial drag force is determined from the Ishii drag model [29], with the drag coefficient determined as follows:

$$C_D = \min\left(C_{D,vis}, C_{D,dis}\right) \tag{10}$$

Here, $C_{D,vis}$ and $C_{D,dis}$ are the drag coefficients in the viscous and distorted regimes, respectively given by [26]:

$$C_{D,vis} = \frac{24}{Re}(1 + 0.15Re^{0.75}) \tag{11}$$

$$C_{D,dis} = \frac{2}{3}\left(\frac{d_p}{\sqrt{\frac{\sigma}{g|\rho_q - \rho_p|}}}\right) \tag{12}$$

where, *σ* is the surface tension, and *Re* the relative Reynolds number.

The lift force is determined by [26]:

$$\vec{F}_{lift,q} = -C_l\rho_q\alpha_p\left(\vec{u}_q - \vec{u}_p\right) \times \left(\nabla \times \vec{u}_q\right) \tag{13}$$

where, C_l is the lift coefficient determined with the modified Tomiyama model by Frank et al. [30],

$$C_l = \begin{cases} min\left[0.288\tanh\left(0.121Re_p\right), f(Eo')\right], & Eo' \le 4 \\ f(Eo'), & 4 < Eo' \le 10 \\ -0.27, & 10 < Eo' \end{cases} \tag{14}$$

where,

$$f(Eo') = 0.00105{Eo'}^3 - 0.0159{Eo'}^2 - 0.0204Eo' + 0.474 \tag{15}$$

and Eo' is a modified Eotvos number

$$Eo' = \frac{g(\rho_q - \rho_p)d_h^2}{\sigma} \tag{16}$$

with,

$$d_h = d_p(1 + 0.163Eo^{0.757})^{\frac{1}{3}} \tag{17}$$

$$Eo = \frac{g(\rho_q - \rho_p)d_p^2}{\sigma} \tag{18}$$

The wall lubrication force is determined by [26]:

$$\vec{F}_{wl} = C_{wl}\rho_q\alpha_p\left|(\vec{u}_q - \vec{u}_p)\right|^2\vec{n}_w \tag{19}$$

where, $\vec{n}_w$ is the unit normal pointing away from the wall, and C_{wl} the wall lubrication coefficient determined by the Antal et al. model [31]:

$$C_{wl} = max\left(0, \frac{C_{w1}}{d_p} + \frac{C_{w2}}{y_w}\right) \tag{20}$$

with, $C_{w1} = -0.01$, $C_{w2} = 0.05$, and y_w the distance to the nearest wall.

The turbulent dispersion force is determined by the Lopez de Bertodano model [32]:

$$\vec{F}_{td,q} = -\vec{F}_{td,p} = C_{TD}\rho_q k_q \nabla\alpha_p \tag{21}$$

where, k_q is the turbulent kinetic energy of the primary phase.

The virtual mass force is determined with the following correlation [26]:

$$\vec{F}_{vm} = C_{vm}\alpha_p\rho_q\left(\frac{d_q\vec{u}_q}{dt} - \frac{d_p\vec{u}_p}{dt}\right) \tag{22}$$

with, $C_{vm} = 0.5$.

The turbulence production and dissipation rate source terms in Eq. (4) and Eq. (5), respectively, are determined with the Troshko-Hassan turbulence interaction model [33]. The turbulence production source term becomes

$$S_{k,m} = C_{ke}K_{pq}\left|\vec{u}_p - \vec{u}_q\right|^2 \tag{23}$$

where, $C_{ke} = 0.75$ and K_{pq} is the fluid-fluid interphase exchange coefficient given as follows:

$$K_{pq} = \frac{\rho_p f}{6\tau_p}d_p A_i \tag{24}$$

with, f the drag function and τ_p the particulate relaxation time. The dissipation rate source term becomes

$$S_{\varepsilon,m} = C_{td}\frac{1}{\tau_p}S_{k,m} \tag{25}$$

with, $C_{td} = 0.45$ and τ_p the characteristic time of the induced turbulence,

$$\tau_p = \frac{2C_{VM}d_p}{3C_D|\vec{u}_p - \vec{u}_q|} \tag{26}$$

2.4 RPI wall boiling model

The RPI wall boiling model of Kurul and Podowski [34] was developed to predict the boiling heat transfer in the subcooled nucleate boiling regime. It partitions the total wall heat flux ($q_W^{"}$) going into the liquid into three components, namely the liquid convective heat flux ($q_C^{"}$), quenching heat flux ($q_Q^{"}$), and evaporative heat flux ($q_E^{"}$),

$$q_W^{"} = q_C^{"} + q_Q^{"} + q_E^{"} \tag{27}$$

In the subcooled boiling regime, the liquid convective heat flux is determined by the following correlation,

$$q_C^{"} = h_C(T_w - T_l)(1 - A_b) \tag{28}$$

where, h_C is the convective heat transfer coefficient derived from the log-law, T_w is the wall temperature and T_l is the liquid temperature determined with a wall function to adhere to the log-law. A_b is the area of influence and represents the portion of the wall that is covered by nucleating bubbles. The portion of the wall covered by liquid is thus represented by $(1 - A_b)$.

The quenching heat flux models the cyclic averaged transient heat transfer caused by liquid filling the void after a bubble departures from the wall. The quenching heat flux is determined as [26]:

$$q_Q^{"} = C_{wt}\frac{2k_l}{\sqrt{\pi\lambda_l t}}(T_w - T_l)A_b \tag{29}$$

where, C_{wt} is the bubble waiting time coefficient with a default value of 1, k_l is the liquid phase thermal conductivity, λ_l the liquid phase diffusivity, and *t* is the periodic time. The quenching heat flux is highly dependent on T_l, resulting in high mesh sensitivity in the near-wall region. Since the standard wall function approach is used, it is desired that the cells adjacent to the wall adhere to $30 < y^+ < 300$, limiting the minimum cell size in mesh refinement. In order to alleviate mesh dependence, T_l is evaluated at a fixed y^+ of 250 as proposed by Egorov and Menter [35].

The evaporative heat flux models the heat transfer causing vapour bubble formation at the wall. The evaporative heat flux is determined as follows [26]:

$$q_E^{"} = \frac{\pi}{6}D_w^3 N_w \rho_v h_{fg} f \tag{30}$$

where, D_w is the vapour bubble departure diameter, N_w is the nucleation site density, ρ_v is the vapour density, and f is the bubble departure frequency.

The area of influence is determined with the following correlation [26]:

$$A_b = min\left(1, K\frac{N_w \pi D_w^2}{4}\right) \tag{31}$$

The upper bound of 1 is imposed on the area of influence to avoid numerical instabilities caused by unbound empirical approximations. Here, K is an empirical constant given by Del Valle and Kenning [36]:

$$\mathrm{K} = 4.8e^{\left(-\frac{Ja_{sub}}{80}\right)} \tag{32}$$

where, Ja_{sub} is the subcooled Jacob number,

$$Ja_{sub} = \frac{\rho_l C_{pl} \Delta T_{sub}}{\rho_v h_{fg}} \tag{33}$$

with, $\Delta T_{sub} = T_{sat} - T_l$.

The frequency of bubble departure is determined by the Cole [37] correlation for saturated pool boiling,

$$f = \frac{1}{t} = \sqrt{\frac{4g(\rho_l - \rho_v)}{3\rho_l D_w}} \tag{34}$$

It should be noted that the Cole correlation is based on the inertia growth of the vapour bubble, which is not occur in subcooled boiling. However, studies [21, 23] have shown that using it for low degrees of subcooling can still produce acceptable results. The nucleation site density as a function of wall superheat is modelled as follows [26]:

$$N_w = C^n (T_w - T_{sat})^n \tag{35}$$

where, $C = 210$ and $n = 1.805$ are empirical constants reported by Lemmert and Chawla [38]. The accurate prediction of the bubble departure diameter is very important in boiling simulations as the evaporation heat flux is highly dependent on the bubble departure diameter. The Unal relation [39] is used in the present study as it is not only based on empirical coefficients but considers wall superheat, amount of subcooling, as well as the local pressure. The bubble departure diameter is determined as follows:

$$D_w = 2.4210^{-5} p^{0.709} \left(\frac{a}{b\sqrt{\varphi}}\right) \tag{36}$$

with,

$$a = \frac{T_w - T_{sat}}{2\rho_v h_{fg}} \sqrt{\frac{\rho_s C_{ps} k_s}{\pi}} \tag{37}$$

$$b = \begin{cases} \dfrac{\Delta T_{sub}}{2\left(1 - \dfrac{\rho_v}{\rho_l}\right)} e^{\left(\frac{\Delta T_{sub}}{3} - 1\right)} \; for \; \Delta T_{sub} \leq 3 \\ \dfrac{\Delta T_{sub}}{2\left(1 - \dfrac{\rho_v}{\rho_l}\right)} \; for \; \Delta T_{sub} \geq 3 \end{cases} \tag{38}$$

$$\varphi = max\left(\left(\frac{U_b}{0.61}\right)^{0.47}, 1.0\right) \tag{39}$$

where, U_b is the near wall bulk velocity, h_{fg} is the latent heat of vaporization and subscripts *s*, *l* and *v* denote the solid, liquid and vapour phases, respectively.

2.5 Solution method

The phase-coupled SIMPLE algorithm is implemented in the present study to achieve pressure-velocity coupling. Spatial discretisation is achieved with the first-order UPWIND method. The pressure is determined with the PRESTO! (PREssure STaggered Option) scheme. Time discretisation is achieved with the first-order implicit method which is unconditionally stable, however, the single-phase Courant number is kept below one to ensure optimal convergence and solution accuracy. Body forces as well as volume fractions are solved implicitly. To further enhance convergence, truncated forms of the virtual mass force is used in cells where convergence issues are present. To limit heat transfer fluctuations caused by the drastic variation in the thermal properties and density of the fluid close to the heated surface due to phase change, a numerical noise filter is applied to the energy equation. All results presented in this paper are time-averaged results determined after the surface temperatures have levelled off and a steady state was reached. To illustrate how steady state was achieved and the time-averaging was performed, Fig. 5 shows the raw simulation data for the full boiling curve produced for the case in Fig. 3. It is shown that for the case in Fig. 3, the heat flux was ramped up after every 10 seconds of simulation flowtime, to allow enough solution flowtime for the average wall temperature to stabilise and reach a steady state. Data averaging was performed by only using the second half (5 seconds for the case shown in Fig. 5) of the heating window. All cases presented in this paper used a similar approach and for cases where conjugate heat transfer in the solid copper block were considered, the heating window was increased to ensure that the average wall temperature reached steady state before time-averaging the data.

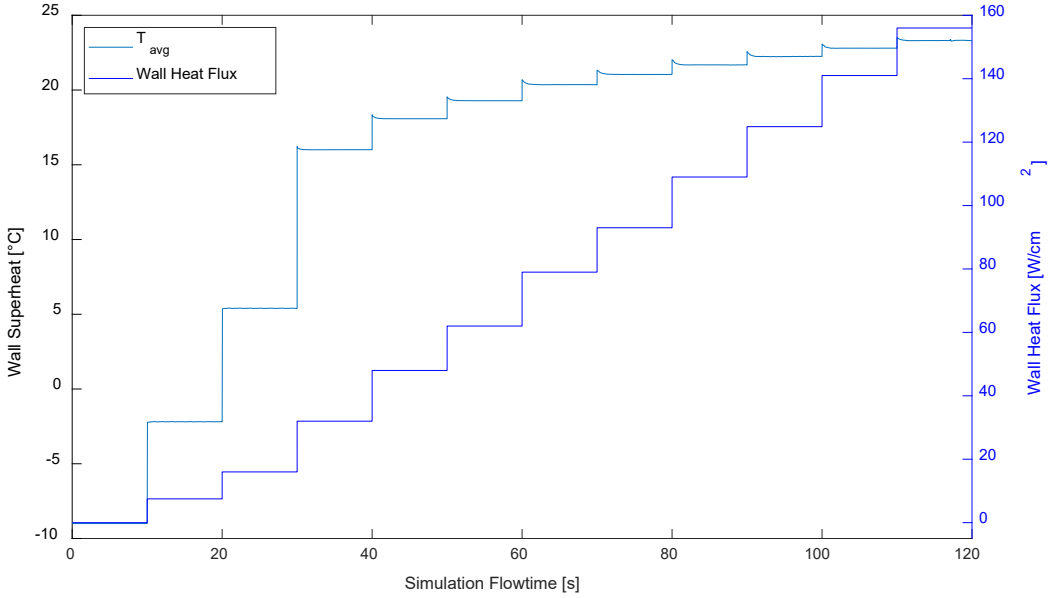

Fig. 5. Area weighted average wall superheat and wall heat flux vs simulation flowtime for 3D multi-jet array without conjugation.

3 Experimental Validation

In this section, the numerical model is validated against published results of two experimental studies of submerged and confined jets in the subcooled nucleate boiling regime. The first validation case considers a single submerged jet, while the second validation case considers a confined jet array.

3.1 2D Axisymmetric single jet

We consider the 2D axisymmetric computational domains mimicking the experiments of Katto and Kunihiro [11] without and with conjugation illustrated in Fig. 1 and Fig. 2, respectively. It is important to note the addition of the hydrostatic pressure gradient to the radial outlet pressure boundary; failure to add it results in convergence issues for the continuity equation. The stagnation region is defined as

the area directly below the jet with the same area as the nozzle exit. The Ranz-Marshall correlation for the liquid side heat transfer coefficient is used for this case. The properties of water at atmospheric pressure are summarised in Table 1.

Table 1: Properties of water at 1 atmospheric pressure

	Water	
	Liquid	Vapour
Saturation temperature (°C)	100	
Surface tension (N/m)	0.059	
Latent heat (J/kg)	2257000	
Density (kg/m^3)	958	0.6
Specific heat (J/kg·K)	4219	2010
Dynamic viscosity (N·s/m^2)	0.000283	0.0000123
Thermal conductivity (W/m·K)	0.68	0.025

3.1.1 Mesh Independence

Since wall functions are used for near-wall treatment, the mesh must satisfy the $y^+ \geq 30$ condition at the walls. As the flow has no velocity at the stagnation point and very low velocities in the stagnation region, meshing the stagnation region with $y^+ < 30$ cannot be avoided. Five consecutively refined meshes with quadrilateral cells with mesh densities ranging from 19.5 cells/mm^2 to 533 cells/mm^2 (cell counts ranging 1950 cells to 53336 cells) were tested for the case without conjugation at a heat flux of 50 W/cm^2 to evaluate mesh dependency. The boundary layer cell thickness is kept constant in all meshes to keep $y^+ \approx 30$ outside the stagnation region. The aspect ratio of all five meshes are kept below 10. The average wall temperature varied around 1% and the stagnation region wall temperature varied around 0.1% when going from mesh density of 121 cells/mm^2 to 533 cells/mm^2. Therefore, mesh density of 121 cells/mm^{2}was deemed sufficient to predict the boiling curve. The case with conjugation used the same mesh density for the fluid and solid regions.

3.1.2 Experimental Validation

The copper impingement disk used in the experiments of Katto and Kunihiro [11] was embedded with four thermocouples, distributed along the axis of the copper block including the jet centreline. The thermocouple readings in conjunction with the one-dimensional heat conduction equation determined the wall temperature as well as the wall heat flux. This suggests that the boiling curve of the experiments is effectively based on the stagnation point wall temperature as noted by Narumanchi et al. [21] and Qui et al. [23], rather than the average wall temperature. Fig. 6 shows the predicted boiling curves for cases with/out conjugation are plotted alongside data from those experiments and those from previous numerical studies [21, 23]. The boiling curves based on the area-weighted average temperature of the stagnation region. The results with conjugation agree well with the experimental data, but the boiling curve shifts to the left when conjugation is not considered. This indicates the importance of considering the effects of conjugate heat transfer. In addition, the presence of the solid copper leads to less variation in the temperature profile of the heated surface (not shown). It must also be noted that our results without conjugation agree well with numerical results of Narumanchi et al. [21].

The small deviations from previous numerical investigations [21, 23] is due to the differences in the models used. We use the Tomiyama lift force model, applicable to deformable bubbles, whereas Narumanchi et al. used the Moraga et al. [40] lift force model, which is mainly applicable to solid spherical particles. Unlike us, Narumanchi et al. [21] also did not evaluate the liquid temperature, used to determine the quenching heat flux at $y^+ = 250$ (as proposed by Egorov and Mentor [35]). Qiu et al. [23] used modifications to the standard *k-ε* model as opposed to the *RNG k-ε* model used here. Also, the interphase transfer models used in the Qiu et al. study were not disclosed, causing some uncertainty in the comparison.

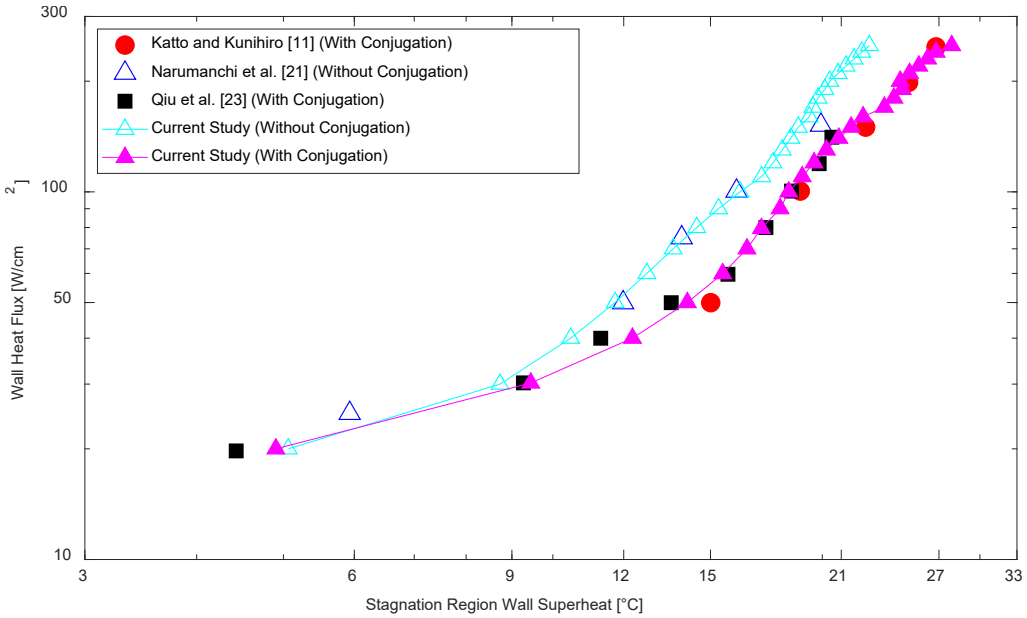

Fig. 6. Boiling curve validation for the Katto and Kunihiro experiment [11] using the stagnation region wall temperature.

3.2 3D Jet array

We consider the Devahdhanush and Mudawar [25] study as presented in Fig. 3 and Fig. 4, without and with conjugation, respectively. Again, note the hydrostatic pressure gradient distribution at the side outlet (Fig. 3b and Fig. 4b). The quarter of the domain that is modelled is shown by the two burgundy lines (symmetry planes) in Fig. 3a and Fig. 4a. R134a exits the jet nozzles at a velocity of 4.01 m/s at a pressure of 771278 Pa with 9°C of subcooling, that translates to an inlet temperature of 20.14°C. The properties of R134a at the saturation pressure are summarised in Table 2. Note that the saturation pressure differs from the one in the experiment, since, the pressure corresponding to a saturation temperature of 29.14°C in Coolprop [41] is slightly different from the one listed in the experiment [25]. The fiberglass properties used for the insulation in the present study are listed in Table 3. The properties of the fiberglass insulation used in the experiment are unknown.

Table 2: Properties of R134a at saturation pressure [41]

Fluid	R134a			
Saturation Pressure (Pa)	751340			
Saturation temperature (°C)	29.14			
Surface tension (N/m)	0.0075			
	Liquid			**Vapour**
Temperature (°C)	**20.14**	**25**	**29.14**	**29.14**
Density (kg/m^3)	1224.82	1206.71	1190.82	36.60
Specific heat (J/kg·K)	1405.9	1423.4	1446.5	1059.44
Dynamic viscosity (N·s/m^2)	2.0701E-04	1.9489E-04	1.8510E-04	1.1869E-05
Thermal conductivity (W/m·K)	0.0832	0.0811	0.0794	0.0142
Specific enthalpy (J/kg)	227665	234546	240481	414399

Table 3: Properties of fiberglass

Solid	Fiberglass
Density (kg/m^3)	1749.3
Specific heat (J/kg·K)	1115
Thermal conductivity (W/m·K)	0.72079

3.2.1 Mesh independence

As in the previous case, the mesh must satisfy the $y^+ \geq 30$ at the walls since standard wall functions are used. To investigate mesh independence, four consecutively refined meshes with polyhedral cells with mesh densities ranging from 25.32 cells/mm^3 to 130.83 cells/mm^3 (cell counts ranging from 126 858 cells to 655 370 cells) were tested for the case without conjugation at an applied heat flux of 80 W/cm^2. Prism boundary layer mesh refinement was used to keep the boundary layer cell thickness constant and $y^+ \approx 30$ for the heated surface outside the stagnation regions. The maximum aspect ratio of the meshes were again kept below 10. The average wall temperature varied by less than 0.3% going from mesh density of 65 cells/mm^3 to 130.83 cells/mm^3. Therefore, the mesh density of 65 cells/mm^3 with 325840 cells was used for the prediction of the boiling curve in the nucleate boiling regime. The case with conjugation used the same mesh parameters for the fluid region and the solid region. It should be noted that mesh independence could be reached by using the default standard wall functions, therefore not requiring the evaluation of T_l at a fixed $y^+ = 250$ [35].

3.2.2 Experimental Validation

The copper block in the experimental study [25] only had one layer of three thermocouples located 6.35 mm below the heated surface. The (area-weighted) average temperature and heat input in the copper block were used with the one-dimensional heat conduction equation to approximate the temperature of the heated surface in the experiment. The heat flux to the fluid for the non-conjugation model was taken to be the same as the reported heat input into the copper block. Since there was only one layer of thermocouples present in the experiment, there is some uncertainty in the heat flux and surface temperature results given that the heat spreading from the copper block into the insulation housing was not accounted for. In addition, an experimental measurement uncertainty of $\pm$2.05% for the heat flux was reported by [25].

The boiling curve predictions of both cases in the present study are plotted with the boiling curve results of the experimental study in Fig. 7. The effect of conjugation in the numerical model is much less than in the single jet case. The simulations agree with the experiment, with a maximum error of 21% due to a small overprediction of the nucleate boiling regime slope of the boiling curve, and of the onset of nucleate boiling departure point. Narumanchi et al. [21] stated that errors of up to 30% are acceptable for numerical predictions of jet impingement boiling. The case considering conjugation heat transfer in the solid yielded less variation in the temperature profile of the heated surface. Another possible cause for the overprediction of wall superheat, is the fact that the Cole bubble departure frequency is not suitable for high degrees of subcooled boiling (9°C in this case). When considering conjugation, the heating period to reach a steady state was much longer than that of the 2D axisymmetric case (which had only 3°C of subcooling). The deviation from the experimental data may also be due to the limitations of the RNG k-ε model based on the mixture of the two phases and its ability to capture the turbulence due to jet-to-jet interactions. There is also some uncertainty in the properties of R134a and the actual saturation temperature corresponding to the outlet pressure used in the experiment. Another important consideration is that the standard RPI boiling model is only applicable to the fully developed nucleate boiling regime.

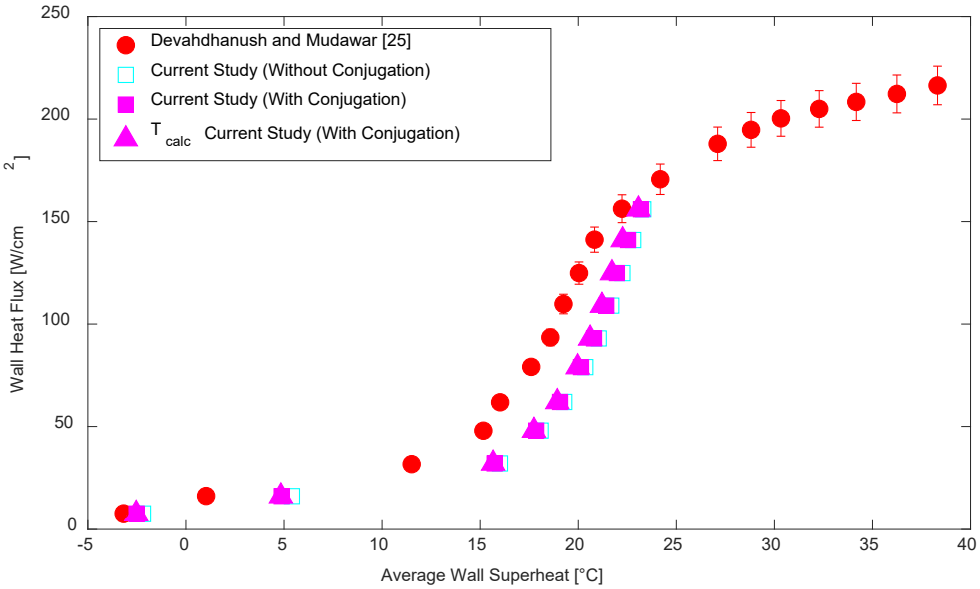

Fig. 7. Boiling curve validation of the numerical model against the experiment of Devahdhanush and Mudawar [25] study using the average heated wall temperature.

4 Results and Discussion

The current study considers two geometries namely, a 2D axisymmetric single round water jet (Fig. 1 and Fig. 2) and a 3D multi jet array using R134a as the heat transfer fluid (Fig. 3 and Fig. 4). Two different heating schemes are used for both cases: i) by means of an isoflux boundary condition as is the case with a thin- film heating source, and ii) by means of conjugate heat transfer though a solid copper block.

4.1 Single axisymmetric water jet

The velocity contours of the single water jet case with conjugation are illustrated in Fig. 8a, with the velocity vector field on top of it. The typical flow regions of jet impingement is visible, i.e., the free jet region, stagnation region and the wall jet region. The wall jet is seen to be expanding as it moves radially along the heated surface, this is due to the vapour formation at the outer edges of the heated surface.

The liquid temperature contours of the single water jet case with conjugation are shown in Fig. 8b, at a heat flux of 50 W/cm^2, which is in the fully developed nucleate boiling regime portion of the boiling curve. The jet is seen to break through the layer of warm liquid above the heated surface to re-wet the surface. The jet then pushes the warm liquid above the surface radially outward which causes the fluid to the outer edges of the heated surface to heat up, allowing for more vapour formation. Further out, the warmer liquid is seen to rise from the heated surface and move back toward the jet centreline. This is due to the jet entrainment causing recirculating flow.

The vapour volume fraction contour plot in Fig. 8c demonstrates that the majority of vapour is formed towards the outer edges of the heated surface. This is due to the lower local convective heat transfer, resulting in more boiling. The vapour is seen to be pushed radially outward by the jet, however, some of the vapour manages to depart up away from the surface before condensing in the subcooled liquid. Almost no vapour is present in and above the stagnation region, this shows that the jet is effective at breaking through the vapour layer above the surface and illustrates why jet impingement extends the nucleate boiling regime (by increasing the CHF).

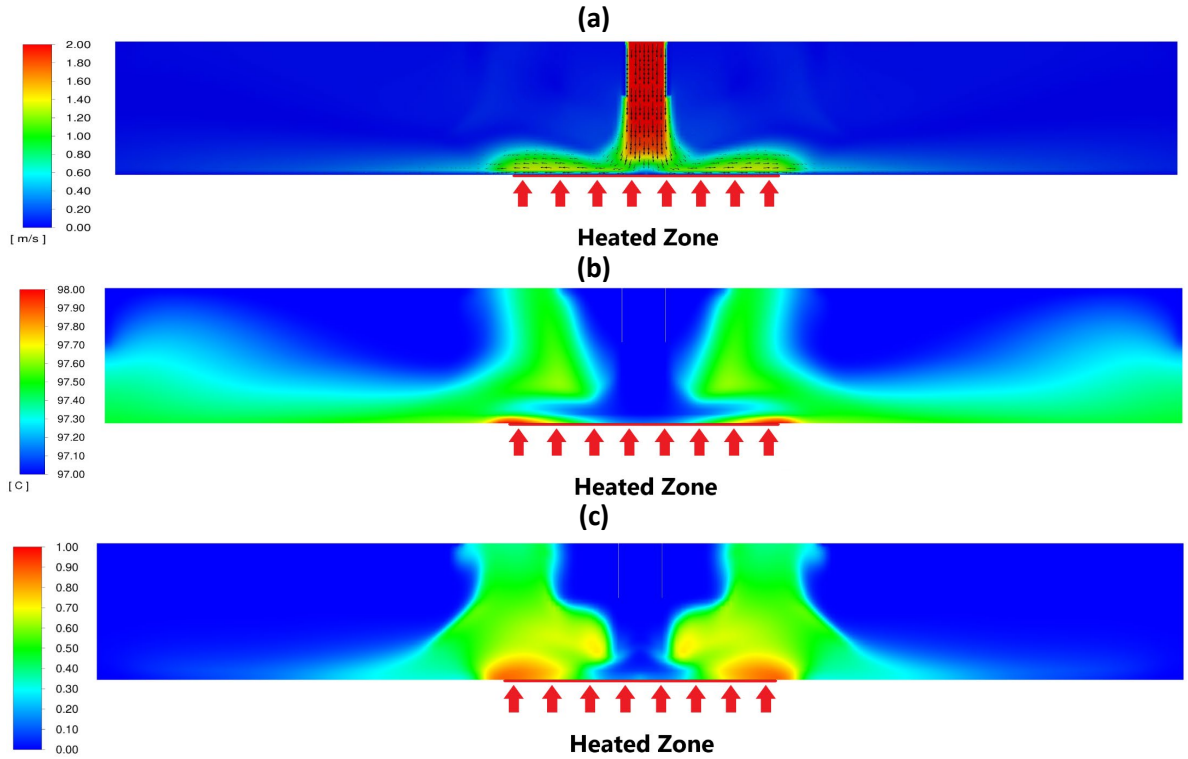

Fig. 8. Single water jet contour plots at 50 W/cm2 applied heat flux. (a) Liquid velocity contours [m/s] with velocity vectors, (b) liquid temperature contours [°C], and (c) vapour volume fraction contours.

The heated wall temperature distribution is shown for various heat fluxes in Fig. 9(a). For all heat fluxes, the wall temperature is a minimum in the stagnation region and increases moving away from the stagnation point. This is due to the fluid heating up as it moves along the heated wall, resulting in lower quenching and convective heat transfer and thus a higher wall temperature. The increase in the wall temperature relative to the stagnation region temperature becomes more significant at higher heat fluxes, this is expected as the outer region of the surface is where dry-out would occur first, due to the wall no longer being wetted (quenching heat transfer).

The heat transfer coefficient distribution is shown for various heat fluxes in Fig. 9(b). The heat transfer coefficient is inversely correlated with the wall temperature, with a maximum heat transfer coefficient in the stagnation region and decreasing moving away from the stagnation point. The drop in heat transfer coefficient relative to the stagnation region becomes more apparent at higher heat fluxes.

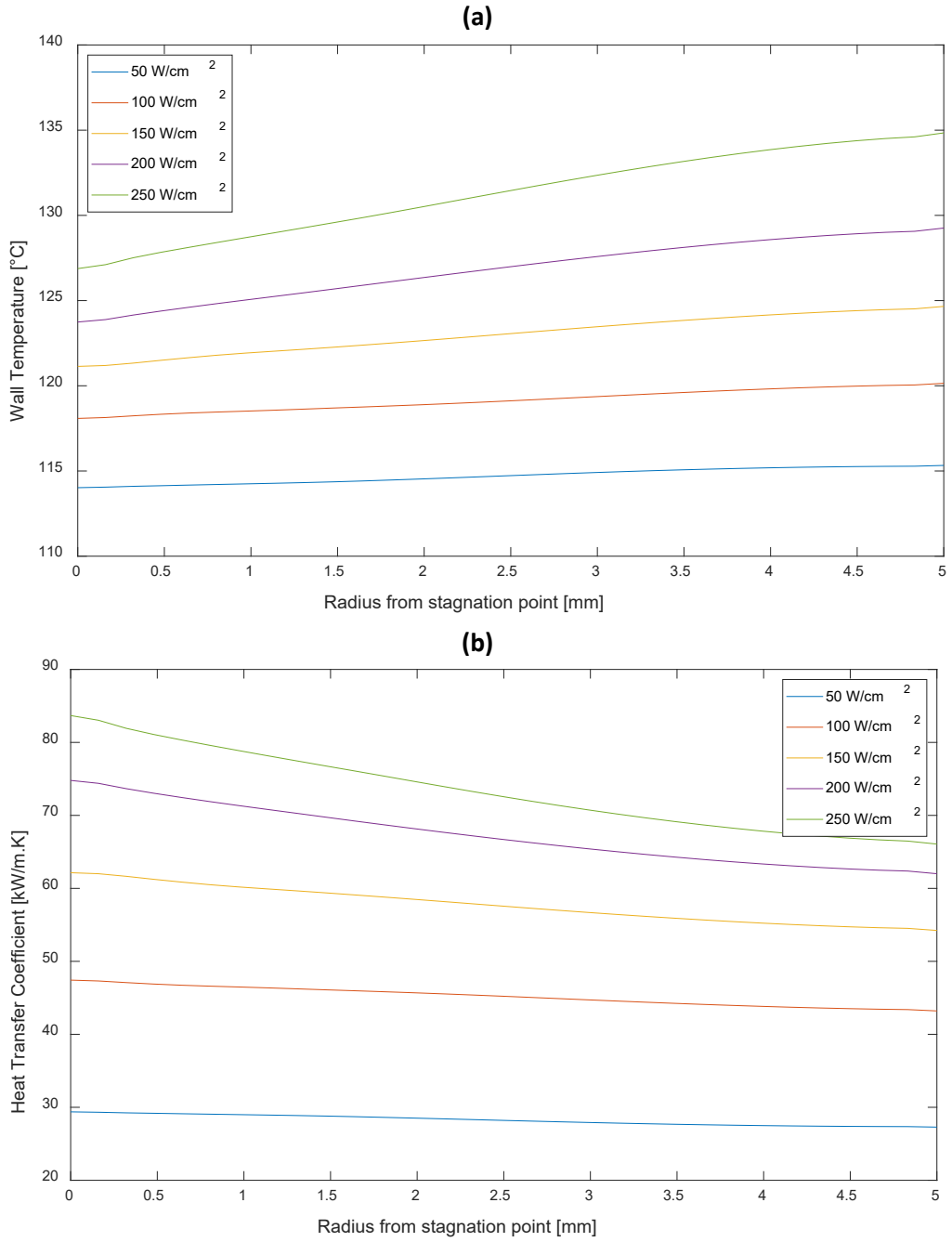

Fig. 9. Single water jet with conjugation at various heat fluxes: (a) wall temperature distribution [°C] and (b) heat transfer coefficient distribution [kW/m^2·K].

4.2 Multi-jet array

The jet velocity contours of the multi-jet array with conjugation are illustrated in Fig. 10a, with the velocity vector field on top of it. The wall jets form a fountain effect where they meet, resulting in additional stagnation regions in-between the jets. The fountain effect can also be observed where the wall jets collide with the side walls of the computational domain, forming additional stagnation regions against the wall. The presence of crossflow is clearly visible in the fountains formed closer to the outlet of the domain. There are also signs of washback from the side wall in the jets closest to the wall, showing a narrower free jet region on the side closest to the wall. The effects of the confinement wall can be observed in the jet fountains washing back down from the top wall into the domain. The effects of confinement are expected to be more severe at higher mass flowrates and lower jet-to-surface spacings.

The liquid temperature contours of the multi-jet array with conjugation are illustrated in Fig. 10b. The effect of the side wall is seen between the side jets and the side wall, with a much higher local liquid temperature than throughout the rest of the array. The presence of crossflow is visible in the trail of warm liquid flowing down the gap between the side jets and side walls. The secondary stagnation regions formed by the colliding wall jets can be seen in the liquid temperature contours as well with a warmer local temperature in the secondary stagnation regions.

The vapour velocity contours on vapour-liquid interface (an iso-surface at a vapour volume fraction of 0.5) are illustrated in Fig. 10c for the multi-jet array case considering conjugation. The vapour velocity is seen to be the highest close to the heated surface in the stagnation region between the jets. This illustrates the influence of the fountain effect on the vapour bubbles. It is also observed that there is minimal vapour in the jet regions indicating that the jets are effective at breaking through the vapour layer above the wall to re-wet the surface. The vapour is seen to move downstream towards the exit of the domain indicating the presence of crossflow. This is also confirmed by the elongation of the vapour bubbles towards the exit of the flow domain.

The wall temperature and heat transfer coefficient contours as calculated from the jet inlet temperature and heated wall temperature are shown in Fig. 11 for the multi-jet array considering the effects of conjugation. The wall temperature reaches a maximum in the wall jet regions and a minimum in the secondary stagnation regions. The minimum wall temperature in the secondary stagnation regions is quite surprising and is expected to be due to the high evaporative heat transfer in these regions where the flow is stagnant. Again the heat transfer coefficient is seen to be inversely correlated to the wall temperature, with the highest heat transfer coefficient occurring in the stagnation regions in the jet centres and mid-way between the jets. This is expected due to the high quenching heat transfer experienced in the jet stagnation regions and high evaporative heat transfer in the regions between the jets. The heat transfer coefficient is seen to be the lowest in the wall-jet regions where boiling heat transfer is the lowest and quenching heat transfer dominates. The wall temperature distribution does not seem to change much with increasing heat flux, Fig. 11a to Fig. 11c. The minimum and maximum surface temperatures do marginally increase with heat flux. Similarly, the heat transfer coefficient distribution does not change much with increasing heat flux, Fig. 11a to Fig. 11c. However, the heat transfer coefficient does increase considerably with increasing heat flux, which is expected due to a drastic increase in heat flux resulting in only a marginal increase in the wall temperature.

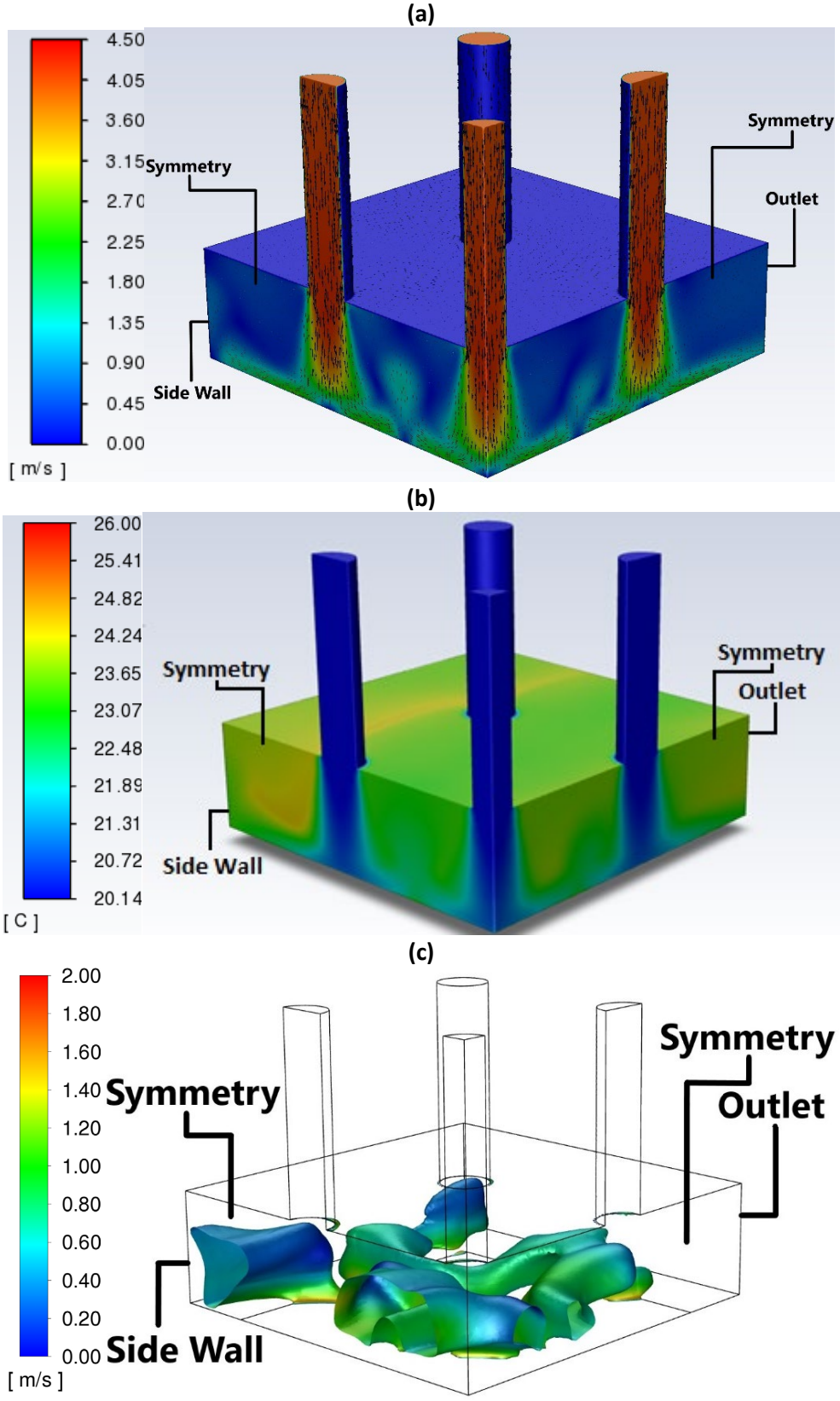

Fig. 10. Contour plots of the multi jet array considering conjugation, using R134a as heat transfer fluid, at a heat flux of 156 W/cm^2. (a) Liquid velocity contours [m/s], (b) liquid temperature contours [°C], and (c) vapour velocity contour on an iso-surface clipped at a vapour volume fraction of 0.5.

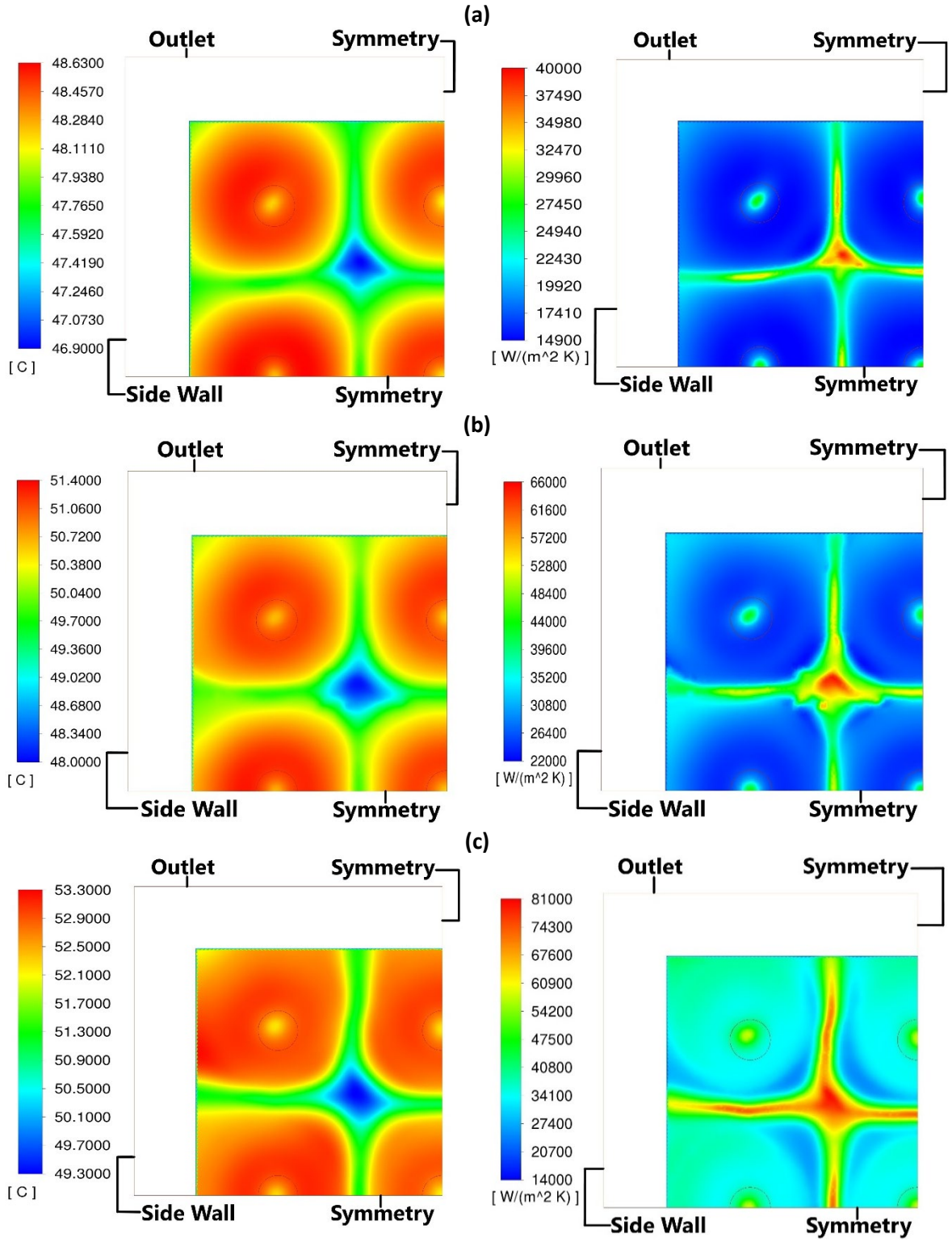

Fig. 11. Heated surface temperature contours [°C] (left) and surface heat transfer coefficient contours [W/m^2·K] (right) of the multi-jet array considering conjugation, using R134a as heat transfer fluid, at various wall heat fluxes: (a) 62 W/cm^2, (b) 109 W/cm^2, and (c) 156 W/cm^2.

4.3 Distributions of vapour

The vapour distribution plots are illustrated in Fig. 12 for the 2D axisymmetric case at various heat fluxes. The vapour fraction in the stagnation region increases with increasing heat flux. It is further seen that the vapour outside the stagnation region also increases with increasing heat flux, however,

is not pushed out radially as far as for the lower heat fluxes. This indicates that the influence of the jet on the vapour is less significant at higher heat fluxes.

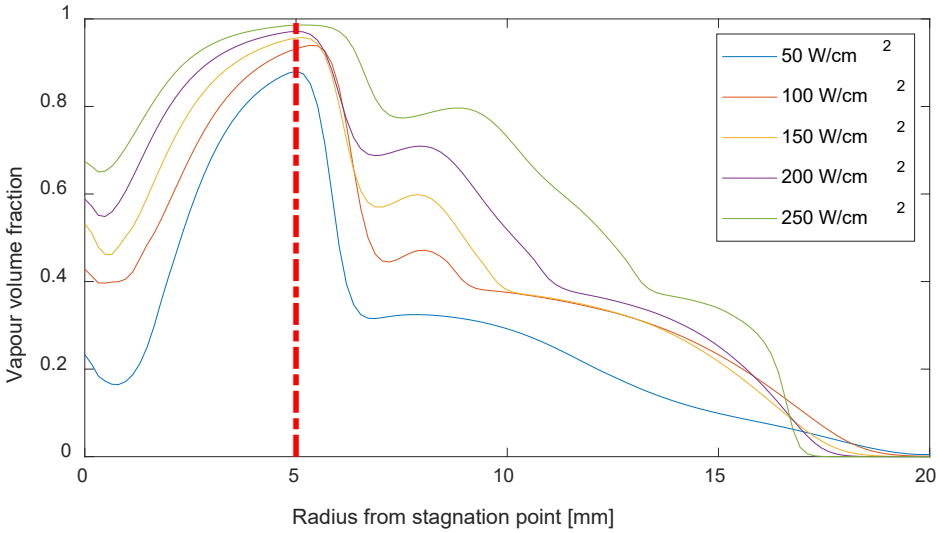

Fig. 12. Vapour distribution plots for 2D axisymmetric case with conjugation at various heat fluxes.

4.4 Effect of conjugation

As mentioned in section 3.1, including the effects of conjugation heat transfer in the heated copper block results in less variation in the heated surface temperature due to the thermal mass of the copper. The minimum, average and maximum surface temperatures are plotted in Fig. 13 for the full boiling curve of the 2D axisymmetric jet for both the case with and without conjugation (Fig. 6). It is seen that the three curves are similar for the case with conjugation than for the case without. This is due to the increased heat transfer into the stagnation region resulting in a lower temperature for the case neglecting conjugation heat transfer. It is also observed that the average surface temperatures for the case with and without conjugation are similar. This suggests that if the average heat transfer performance of jet impingement boiling is of interest, the effects of conjugation heat transfer can be neglected without sacrificing too much accuracy.

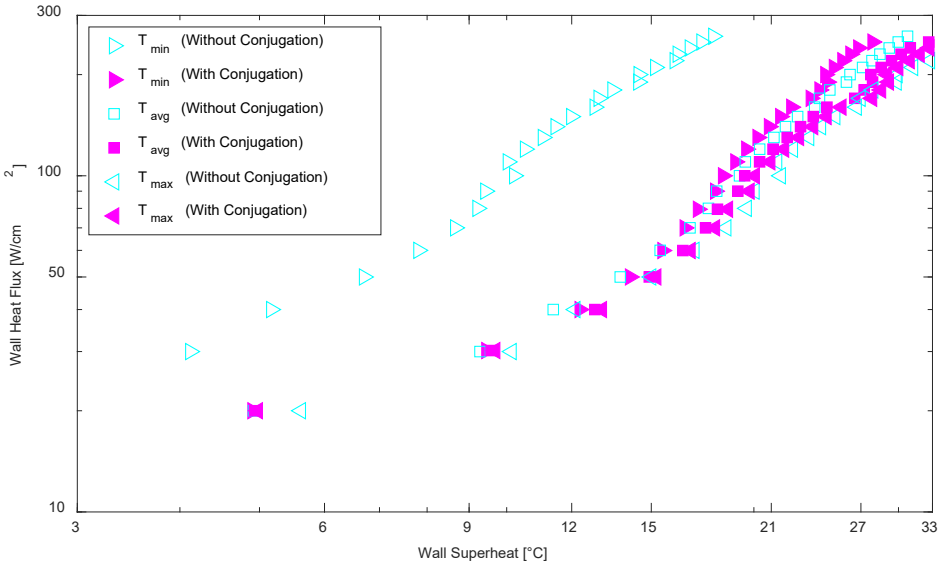

Fig. 13. Single water jet boiling curve based on minimum, average and maximum surface temperatures for both the case without conjugation heat transfer as well as case with conjugation heat transfer.

The boiling curves based on the minimum, average and maximum surface temperatures are plotted in Fig. 14 for the multi-jet array for the case considering conjugate heat transfer as well as the case not considering it (Fig. 7). Similar trends are observed as for the single-jet case.

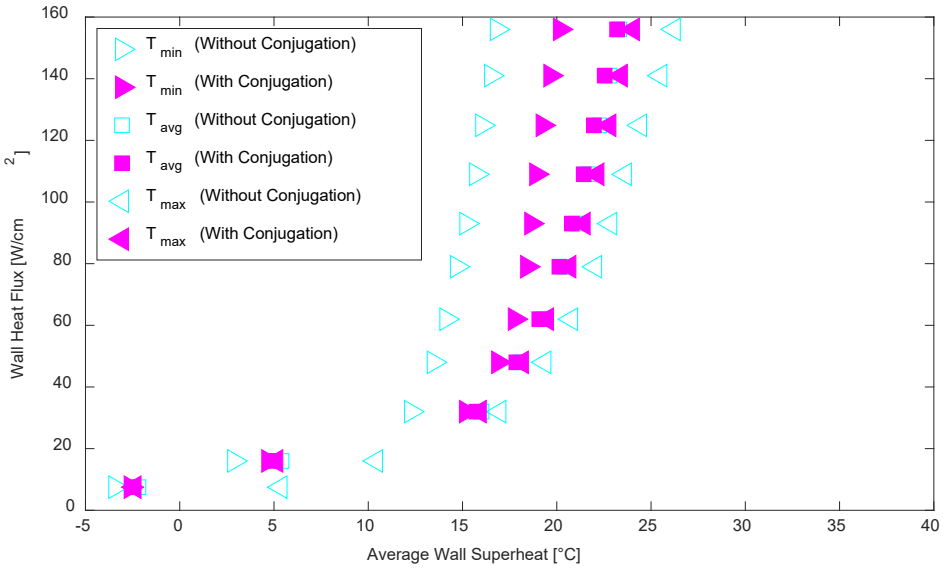

Fig. 14. R134a multi jet array boiling curve based on minimum, average and maximum surface temperatures for both the case without conjugation heat transfer as well as case with conjugation heat transfer.

The contributions of the three heat flux components of the RPI boiling model to the total heat flux (as defined in equations 27 to 30 in section 2.4) are plotted for various applied heat fluxes in Fig. 15 for the 2D axisymmetric case. The evaporative heat flux contribution is higher for the case with conjugation while the quenching heat flux contribution is lower. Compared to the results of Qiu et al. [23], also in the figure, the convective and quenching heat flux contributions of the present study with conjugation is lower while the evaporative heat flux contribution is higher. It is important to note that for the current study, the evaporative heat flux contribution approaches one while the quenching heat flux approaches zero. This suggests that the evaporative heat flux contribution of the RPI boiling model will reach unity at the so-called onset of nucleate boiling departure (ONDB) which marks the end of the fully developed nucleate boiling regime where the standard RPI boiling model is applicable. This is an important observation for design purposes where the ONBD or CHF is not known beforehand.

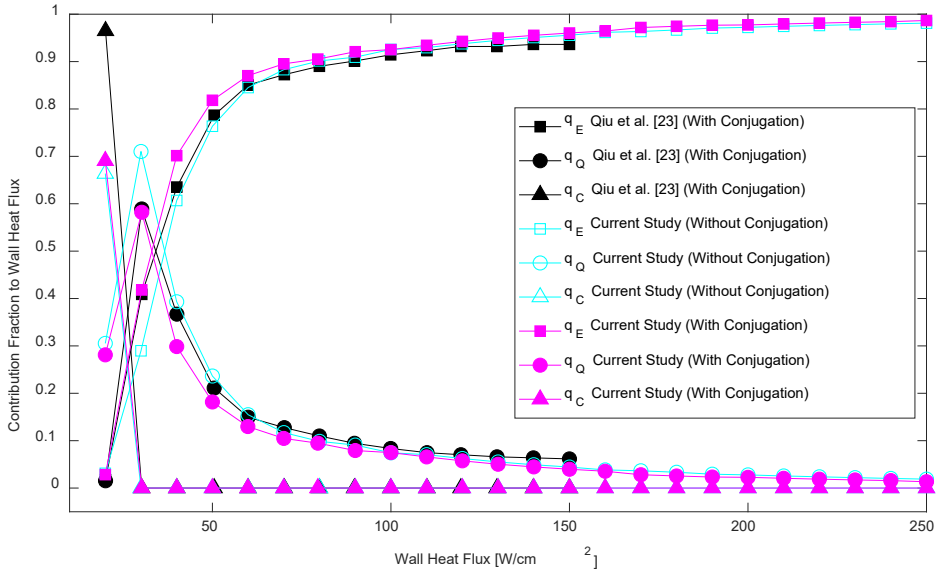

Fig. 15. Contribution of the RPI boiling model heat flux components to the total wall heat flux for the single water jet without and with conjugation heat transfer.

The contributions of the three heat flux components of the RPI boiling model to the total heat flux are illustrated for the boiling curve in Fig. 16 for the multi-jet array case for both the case considering conjugation heat transfer as well as the case not considering it. Compared to the results of the single jet case in Fig. 15, the evaporative heat flux contribution is lower. This makes sense given that the Cole bubble departure frequency model [37] is not applicable to subcooled boiling resulting in lower evaporative heat transfer. The contribution of the evaporative heat flux to the total heat flux only reaches one at a much higher heat flux than the ONBD of the experiment. This suggests Cole bubble departure frequency model [37] should not be used for high degrees of subcooling as it will not correctly predict the ONBD, and will therefore also lead to inaccuracy in predicting the fully developed nucleate boiling regime.

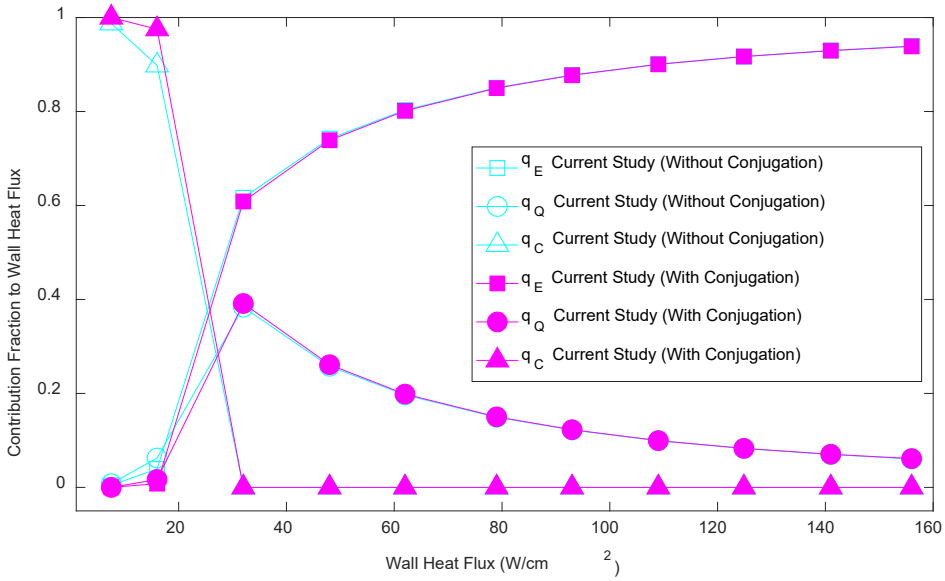

Fig. 16. Contribution of the RPI boiling model heat flux components to the total wall heat flux for the R134a jet array without and with conjugation heat transfer.

4.5 Parametric analysis

To investigate the influence of design parameters on heat transfer, the total heat transfer coefficient (HTC) is defined as:

$$HTC_{Total} = \frac{q_W^{"}}{T_W - T_{in}} \tag{40}$$

Here, $q_W^{"}$ is the total wall heat flux, T_W the average wall temperature, and T_{in} the temperature at the jet inlet. Given that the RPI boiling model approximates the total heat flux with three heat flux components, we define separate heat transfer coefficients for each of the components as below:

$$\begin{aligned} HTC_{Total} = {} & HTC_{Convection} + HTC_{Quenching} + HTC_{Evaporative} \\ & = \frac{q_C^{"}}{T_W - T_{in}} + \frac{q_Q^{"}}{T_W - T_{in}} + \frac{q_E^{"}}{T_W - T_{in}} = \frac{q_W^{"}}{T_W - T_{in}} \end{aligned} \tag{41}$$

where subscripts *C*, *Q* and *E* denote the convective, quenching and evaporative heat flux components, respectively. Given that the focus of the present study is on jets in the fully developed nucleate boiling regime, the convective heat flux is zero for all cases in this section and is not illustrated. All results in this section represent the time-averaged results obtained over at least 20 convective time scales based on the jet velocity and jet-to-surface spacing, i.e., after a quasi-steady state has been reached.

4.5.1 Single jets

To investigate the influence of jet-to-surface spacing and jet Reynolds number on the average heat transfer of a single round water jet, the domain in Fig. 2 used for the validation of the Katto and Kunihiro [11] experiment, is modified by moving the top (free-surface) outlet to 10 jet diameters above the heated surface and varying the jet nozzle exit height to change H/D. The length of the jet pipe upstream of the nozzle exit is kept constant for all H/D cases to ensure that the nozzle outlet velocity profile and turbulence quantities are consistent for all cases. The jet Reynolds number is varied by changing the jet velocity while keeping the diameter constant. Three Reynolds numbers (10000, 15000, 20000) are tested for jet-to-surface spacings of H/D = 1, 2, 4, 8 at a wall heat flux of 50 W/cm^2.

The resulting heat transfer coefficients are provided in Fig. 17. As illustrated in Fig. 17(a), the total heat transfer coefficient increases for increasing H/D for low jet Reynolds numbers, while decreasing for increasing H/D for high jet Reynolds numbers. The influence of impact distance on the total heat transfer coefficient is less apparent at higher Reynolds numbers. This is expected given that there is less jet spreading in the free-jet region and thus less jet decay at higher Reynolds numbers. As a result, at low jet Reynolds numbers and small impact distances, the jet covers only a small portion of the heated surface while at large impact distances, the jet covers a much larger portion of the heated surface due to jet spreading. At high jet Reynolds numbers and small impact distances, the jet has enough kinetic energy to spread out rapidly over the entire heated surface, while the kinetic energy reduces with an increase in the impact distance resulting in less spreading over the heated surface due to the minimal jet spreading in the free-jet region. The quenching heat transfer coefficient illustrated in Fig. 17(b), follows the same trend as the total heat transfer coefficient. The same arguments made for the total heat transfer coefficient holds for the quenching heat transfer coefficient. As illustrated in Fig. 17(c), the evaporative heat transfer coefficient increases with H/D for all jet Reynolds numbers. This suggests that the jet becomes less efficient at wetting the surface with increasing impact distances resulting in higher heat transfer due to phase change.

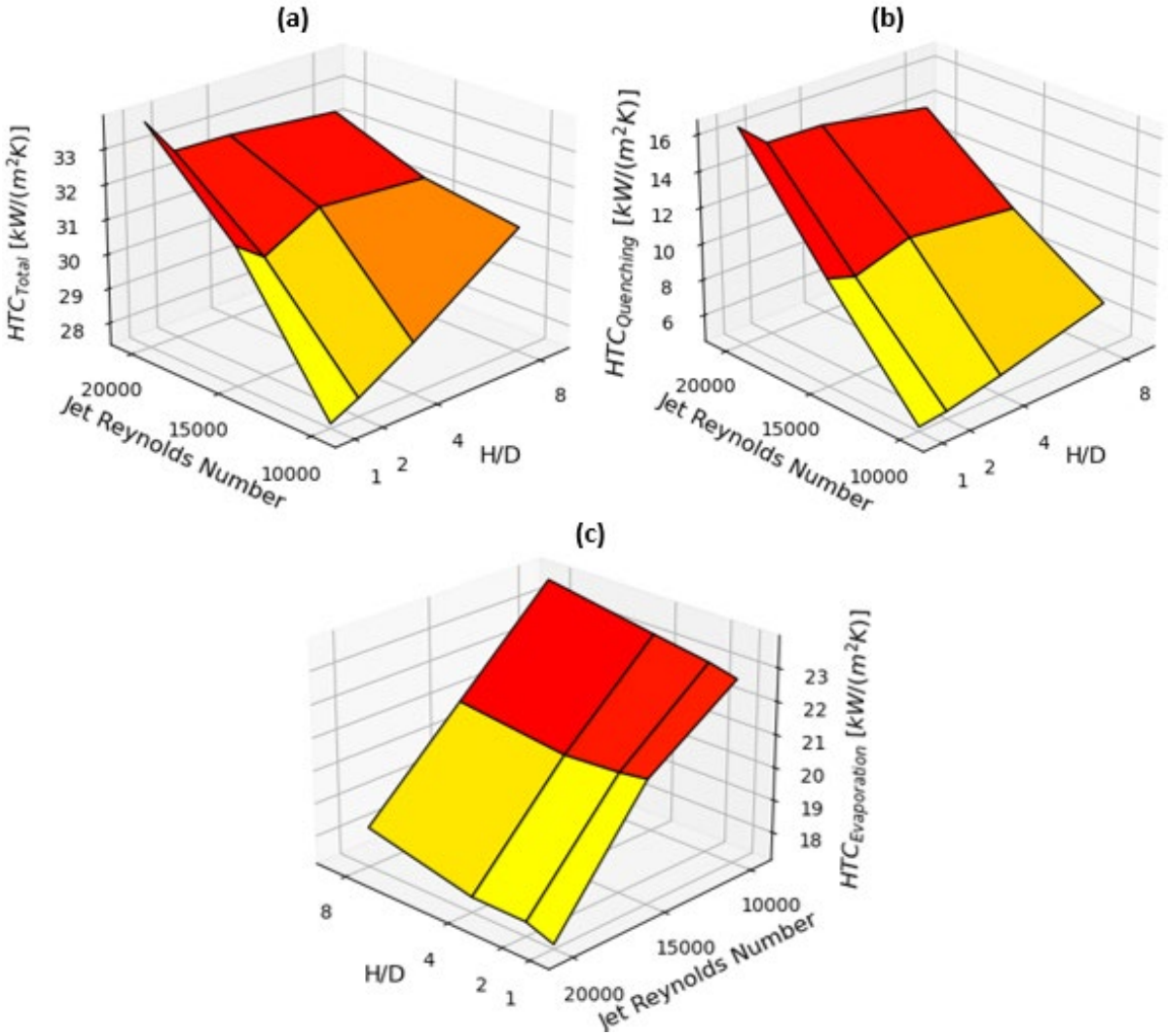

Fig. 17. Heat transfer coefficient (HTC) as calculated for a single water jet as a function of jet Reynolds number (Re) and jet-to-surface spacing (H/D), at 50 W/cm^2 with conjugation: (a) based on the total heat flux, (b) based on the quenching heat flux component, and (c) based on the evaporative heat flux component.

To investigate the influence of jet velocity on the boiling curve, the full boiling curves were produced for the single water jet with H/D = 2 and Re = 10000, 15000, and 20000, corresponding to jet velocities of 1.85 m/s, 2.77 m/s, and 3.69 m/s, respectively. The boiling curves are shown in Fig. 18. The ONB occurs at a higher heat flux for higher jet velocities, indicating an increase in the convective heat transfer with jet velocity, which correlates well with the findings of experiments reported in the literature, such as the findings of Zhou and Ma [13]. The nucleate boiling regime is mostly unaffected by the jet velocity, however, there is a slight shift to the left for increasing jet velocity, indicating improved heat transfer for increasing jet velocity. The difference between the cases is less apparent at higher heat fluxes, where they almost collapse to one curve.

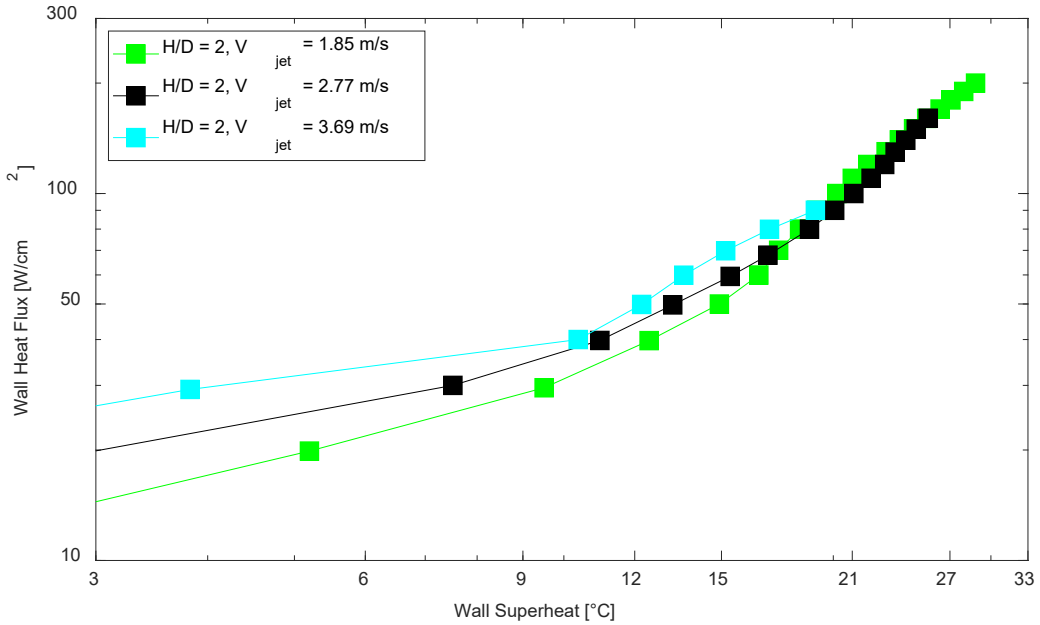

Fig. 18. Boiling curves for a single water jet impinging on a round heated surface, with H/D = 2 for jet Reynolds numbers of 10000, 15000, and 20000, corresponding to jet velocities of 1.85 m/s, 2.77 m/s, and 3.69 m/s, respectively.

4.5.2 Jet arrays

To investigate the influence of jet Reynolds number and jet-to-surface spacing on the average heat transfer of a multi-jet array using R134a as heat transfer fluid, a parametric study is conducted on the geometry illustrated in Fig. 4. Reynolds numbers of 30000, 40000 and 50000 are tested for jet-to-surface spacings of H/D = 1, 2, 4 and 8 at a wall heat flux of 100 W/cm^2. The Reynolds number is varied by varying the jet velocity while keeping the jet diameter constant. The resulting heat transfer coefficients are given in Fig. 19. As illustrated in Fig. 19(a), the total heat transfer coefficient decreases for increasing jet Reynolds numbers at all H/D values. The decrease in the total heat transfer coefficient becomes more apparent at high H/D values. This is somewhat unexpected, however, it may be due to jet-to-jet interactions reducing the effectiveness of the jets. The total heat transfer coefficient is nearly unaffected by the jet Reynolds number for low H/D ratios which aligns with the observations of experimental studies. The quenching heat transfer coefficients are illustrated in Fig. 19(b). The quenching heat transfer coefficient is seen to achieve a maximum at H/D=2 and a minimum at H/D=8. This indicates that jet-to-jet interactions are present and which could explain why the total heat transfer coefficient reduces for increasing jet Reynolds number. The evaporative heat transfer coefficients are illustrated in Fig. 19(c). The evaporative heat transfer coefficient is seen to increase with H/D and decrease with jet Reynolds number. This indicates that the fluid boils more vigorously due to lower quenching heat transfer. It is therefore expected that the critical heat flux would increase with jet Reynolds number and decrease with H/D. It is also expected that the optimal CHF would lie in the region of 1<H/D<2.

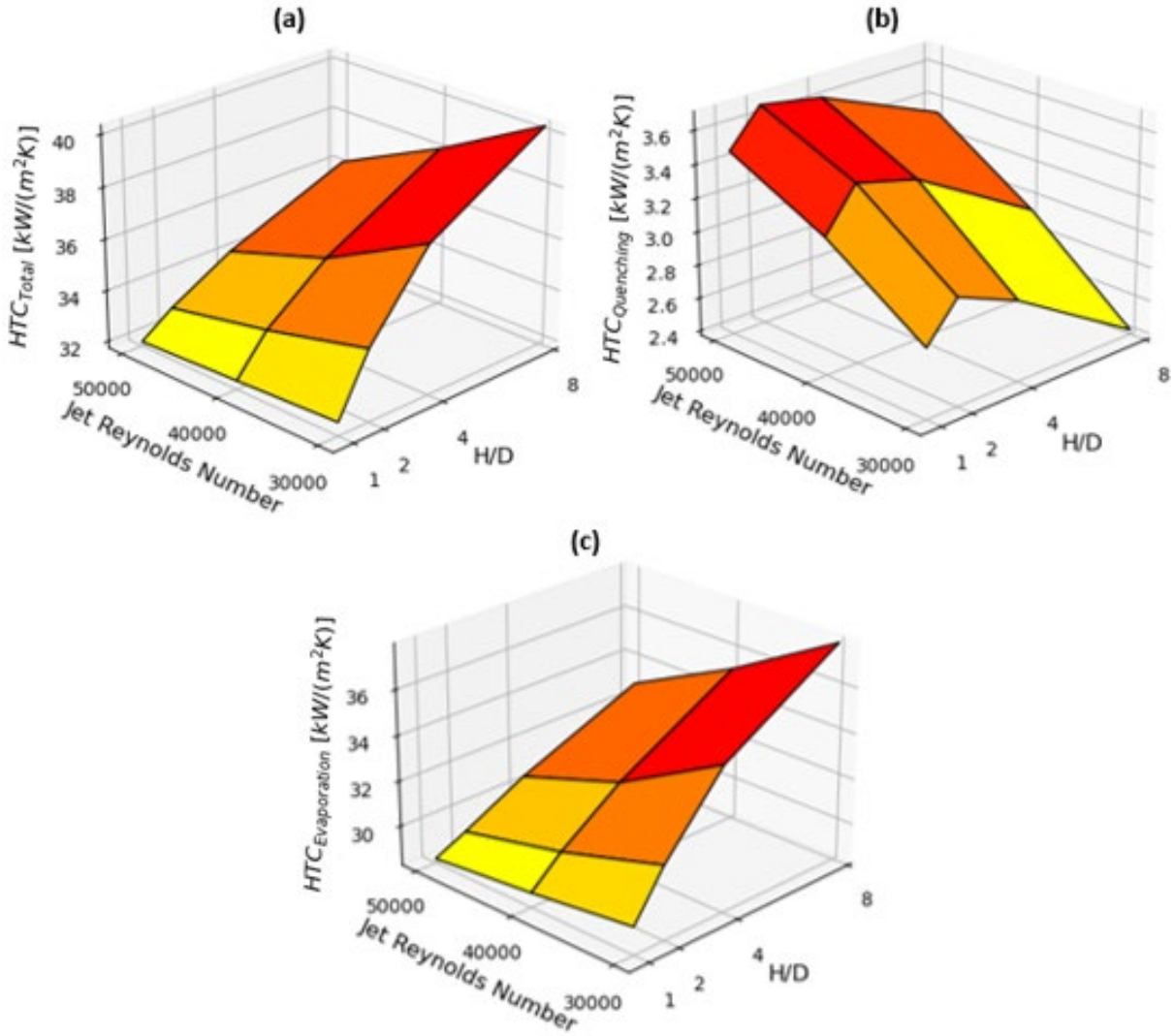

Fig. 19. Heat transfer coefficient (HTC) as calculated for a multi jet array as a function of jet Reynolds number (Re) and jet-to-surface spacing (H/D), at 100 W/cm^2 with conjugation: (a) based on the total heat flux, (b) based on the quenching heat flux component, and (c) based on the evaporative heat flux component.

To investigate the influence of jet velocity on the boiling curve of a jet array, the full boiling curves were produced for the multi-jet array with H/D = 2 and Re = 30000, 40000, and 50000, corresponding to jet velocities of 2.47 m/s, 3.28 m/s, and 4.1 m/s, respectively. The boiling curves are shown in Fig. 20. As for the single water jet, the ONB occurs at a higher heat flux for higher jet velocities, indicating an increase in the convective heat transfer with jet velocity. However, unlike for the single water jet, the nucleate boiling regime is influenced by the jet velocity with a non-constant slope in the fully developed nucleate boiling regime. This result is unexpected and does not agree with the findings of experimental studies, however, is expected to be due to the use of non-constant properties for the jet array case, resulting in different local fluid properties for the different jet velocity cases. The slopes of the boiling curves do become constant at higher heat fluxes on the boiling curve and is expected to be due to the local liquid temperature and thus local fluid properties to stabilise across the different velocity cases.

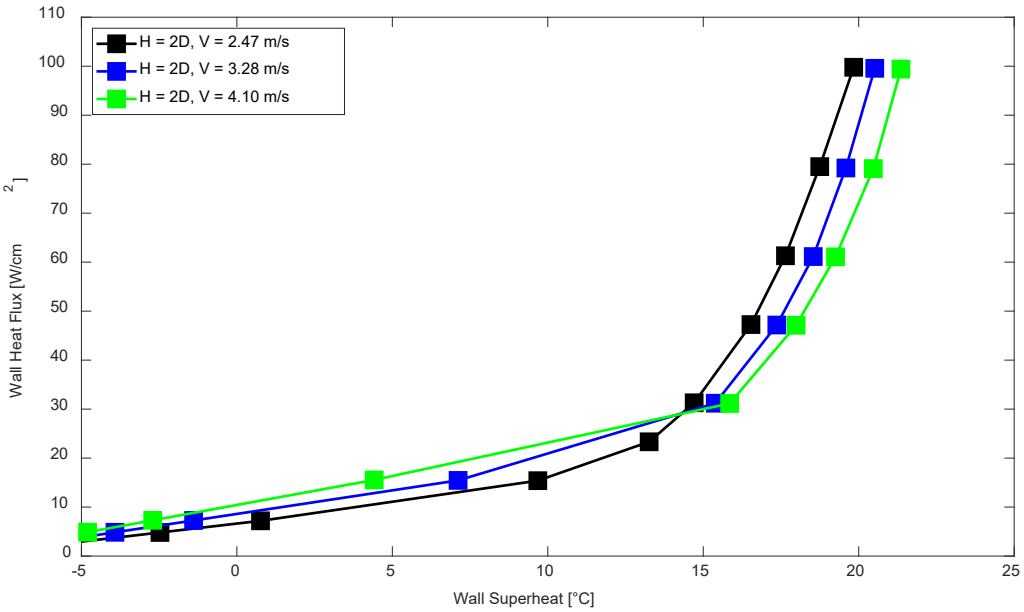

Fig. 20. Boiling curves for a multi-jet array impinging on a square surface, with H/D = 2 for jet Reynolds numbers of 30000, 40000, and 50000, corresponding to jet velocities of 2.47 m/s, 3.28 m/s, and 4.1 m/s, respectively.

4.6 Influence of subcooling on the boiling curve

As was mentioned in section 2.4, the Cole bubble departure frequency model used in the present study was developed for saturated pool boiling and is not applicable to high degrees of subcooling. To investigate the adaptability of the model, the single water jet case with conjugation (illustrated in Fig. 2) and the multi-jet array case with conjugation (illustrated in Fig. 4) were repeated for different degrees of subcooling. It is known from experimental studies that the boiling curve in the fully developed nucleate boiling regime is mostly unaffected by the degree of subcooling, however, the onset of nucleate boiling and CHF is affected by the degree of subcooling. The results of the subcooling study of the single jet and multi-jet cases are shown in Figs. 21 and 22, respectively. For both cases, the heat flux at the ONB increased with subcooling which agrees well with experimental results reported in the literature. For both cases, a clear shift of the boiling curve to the left is observed for lower degrees of subcooling, indicating improved heat transfer for decreasing subcooling. This does not correlate well with the findings of experiments reported in the literature and indicates that the Cole bubble departure frequency model could not be applicable. It is therefore suggested that, before the RPI boiling can be widely implemented in the design process of jet impingement boiling, a bubble departure frequency model insensitive to the degree of subcooling must be developed.

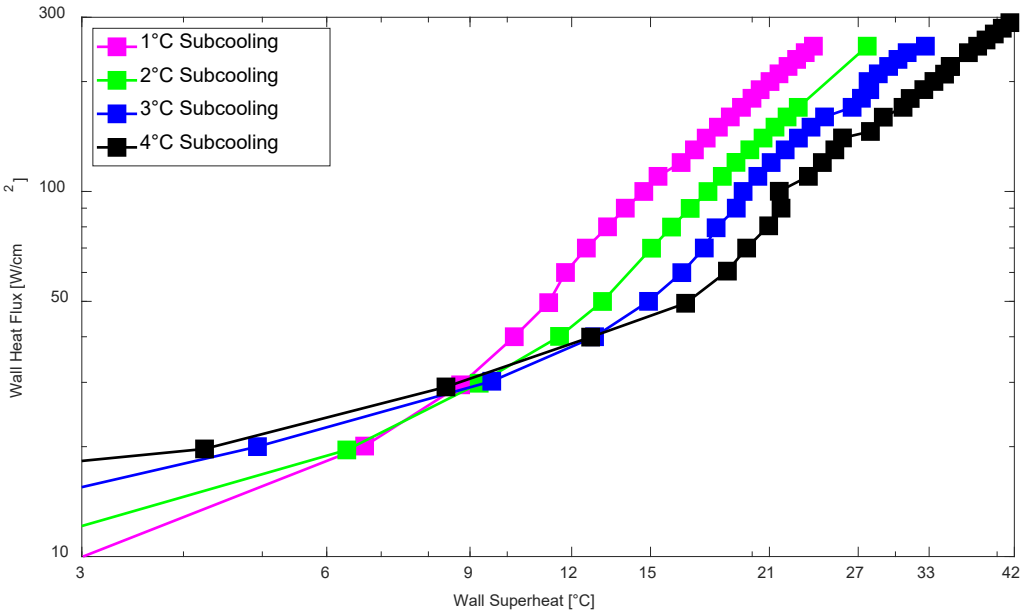

Fig. 21. Boiling curves for the single water jet case with conjugation, based on the area weighted average wall temperature, for various degrees of subcooling.

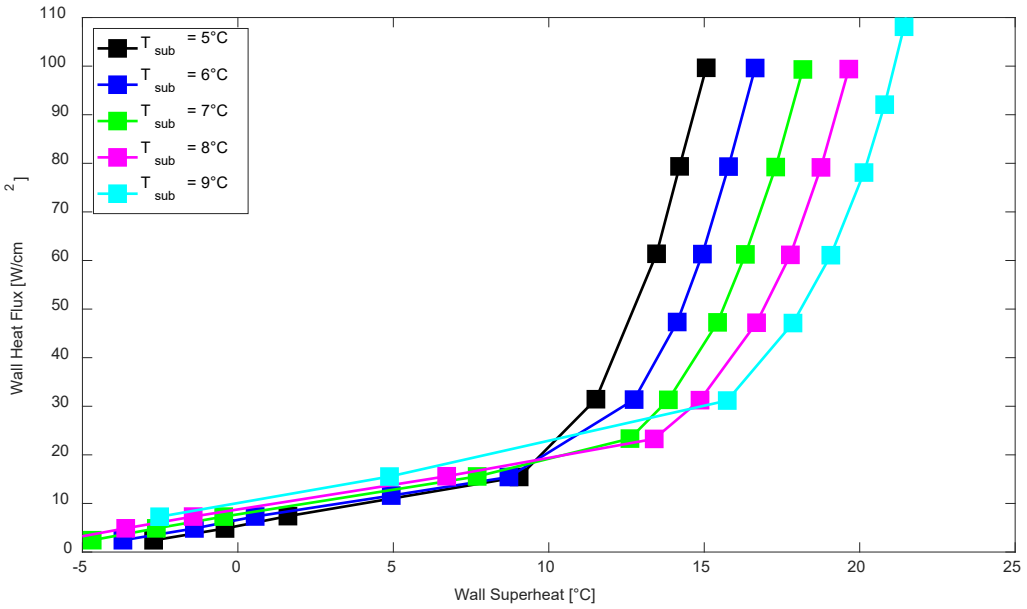

Fig. 22. Boiling curves for the multi-jet array case with conjugation, based on the area weighted average wall temperature, for various degrees of subcooling.

5 Conclusions

The present study involved computational investigations of round jets impinging on heated surfaces in the nucleate boiling regime. Both single and multi-jet arrays were considered. Our working fluids were water and R134a, corresponding to the experiments. Validating numerical models against experiments gave confidence in our modelling ensuring that heat transfer can be successfully predicted. A parametric study presenting the influence of jet Reynolds number and jet-to-surface spacing on the average heat transfer of single and multi-jet arrays has been conducted. Key findings from the study are:

(1.) Conjugate heat transfer in the solid heating block is an important factor to be considered should the heating scheme in the experimental setup have significant thickness and mass.

Ignoring the effects of conjugation could result in inaccurate predictions of surface temperature profile and thus heat transfer coefficient.

(2.) The RPI boiling model can, at most times, successfully predict the ONBD. However, special care should be taken in cases where the ONBD or CHF is not known in advance as the model could fail predict it, which may be detrimental for design purposes.

(3.) For single submerged jets, the total heat transfer coefficient increases with velocity while the evaporative heat transfer coefficient decreases. As a result, the CHF also increases with velocity in agreement with experimental investigations in the literature.

(4.) For single submerged jets, the total heat transfer coefficient increases with jet-to-surface spacing at jet Reynolds numbers $Re = 10000$ but decreases at jet $Re > 10000$. This suggests that an optimal jet-to-surface spacing exists, which aligns with the literature.

(5.) For single submerged jets, the ONB heat flux increases with jet velocity. The boiling curve shifts to the left with increasing jet velocity at low heat fluxes, but collapse on each other at higher heat fluxes, thus the boiling curve is not apparently influenced by jet velocity in the fully developed nucleate boiling regime for higher heat fluxes.

(6.) For confined multi-jet arrays, the total heat transfer coefficient decreases for increasing jet-to-surface spacing for all tested jet Reynolds numbers. However, the total heat transfer coefficient is not a function of jet-to-surface spacing at jet $Re = 50000$. This is because jet-to-jet interactions at increased jet-to-surface spacings are not as strong at these flow rates due to reduced jet spreading. The evaporative heat transfer coefficient increases with jet-to-target spacing at $30000 \leq Re \leq 50000$. The quenching heat flux peaks at $H/D = 2$, which shows that there exists an optimal jet-to-surface spacing resulting in optimal CHF.

(7.) For confined multi-jet arrays, when the total heat transfer coefficient decreases with increasing jet Reynolds numbers, the evaporative heat flux also reduces. As a result, the CHF increases with the jet Reynolds number.

(8.) For confined multi-jet arrays, the ONB is delayed with increasing jet velocity, however, the boiling curve shifts to the left for decreasing jet velocity. Thus, heat transfer in the fully developed nucleate boiling regime decreases with increasing jet velocity.

(9.) For both single submerged jets and confined multi-jet arrays, the ONB heat flux increases with subcooling while the boiling curve shifts to the left for decreasing subcooling.

Acknowledgements

The authors gratefully acknowledge the support received from the ThermaSMART project of the European Commission (Grant: EC-H2020-RISE-ThermaSMART-778104). The authors also acknowledge the Centre for High Performance Computing (CHPC), South Africa, for providing computational resources to this research project.

References

[1] P.K. Singh, Sahu, S.K., Upadhyay, P.K., Jain, A.K., Experimental investigation on thermal characteristics of hot surface by synthetic jet impingement, Applied Thermal Engineering, 165 (2020)(114596).

[2] R. Kumar, Singh, G., Mikielewicz, D., Effect of asymmetric fluid flow distribution on flow boiling in a microchannel heat sink – An experimental investigation, Applied Thermal Engineering, 213 (2022)(118710).

[3] D.B. Marchetto, Ribatski, G., An experimental study on flow boiling heat transfer of HFO1336mxx(Z) in microchannels-based polymeric heat sinks, Applied Thermal Engineering, 180 (2020)(115815).

[4] Y.Y. Liu, Bhaiyat, T.I., Schekman, S.W., Lu, T.J., Kim, T., Impingement cooling of an isoflux flat plate by blockage jet, Applied Thermal Engineering, 209 (2022)(118239).

[5] F. Afroz, Sharif, M.A.R., Numerical study of turbulent annular impinging jet flow and heat transfer from a flat surface, Applied Thermal Engineering, 138 (2018) 154-172.
[6] J. Zhu, Dou, R., Hu, Y., Zhang, S., Wang, X., Heat transfer of multi-slot nozzles air jet impingement with different Reynolds number, Applied Thermal Engineering, 186 (2021)(116470).
[7] I. Mudawar, Recent Advances in High-Flux, Two-Phase Thermal Management, Journal of Thermal Science and Engineering Applications, 5 (2) (2013).
[8] M.J. Rau, S.V. Garimella, Two-phase jet impingement: liquid-vapor interactions and heat transfer mapping for multiscale surface enhancement design, Encyclopedia of Two-Phase Heat Transfer and Flow, 2 (2018).
[9] L. Qiu, S. Dubey, F.H. Choo, F. Duan, Recent developments of jet impingement nucleate boiling, International Journal of Heat and Mass Transfer, 89 (2015) 42-58.
[10] R.J. Copeland, Boiling heat transfer to a water jet impinging on a flat surface (Ph.D. thesis), in, Southern Methodist University, Dallas, TX, 1970.
[11] Y. Katto, M. Kunihiro, Study of the mechanism of burn-out in boiling system of high burn-out heat flux, JSME international journal, 16(99) (1973) 1357-1366.
[12] C.L. Struble, L.C. Witte, An in situ technique for measuring heat transfer from a power transistor to a boiling liquid, Journal of Heat Transfer, 116(2) (1994) 495-498.
[13] D.W. Zhou, C.F. Ma, Local jet impingement boiling heat transfer with R113, Heat Mass Transfer, 40(6-7) (2004) 539-549.
[14] R. Cardenas, V. Narayanan, Heat transfer characteristics of submerged jet impingement boiling of saturated FC-72, International Journal of Heat and Mass Transfer, 55 (2012) 4217-4231.
[15] Z. Zhao, Y. Peles, M.K. Jensen, Water jet impingement boiling from structured-porous surfaces, International Journal of Heat and Mass Transfer, 63 (2013) 445-453.
[16] F.J. Hong, C.Y. Zhang, W. He, P. Cheng, G. Chen, Confined jet array impingement boiling of subcooled aqueous ethylene glycol solution, International Communications in Heat and Mass Transfer, 56 (2014) 165-173.
[17] M.D. Clark, J. A.Weibel, S.V. Garimella, Identification of nucleate boiling as the dominant heat transfer mechanism during confined two-phase jet impingement, International Journal of Heat and Mass Transfer, 128 (2019) 1095-1101.
[18] R. Cardenas, V. Narayanan, Submerged jet impingement boiling of water under subatmospheric conditions, Journal of Heat Transfer 134(2) (2012).
[19] Y. Li, Y. Chen, Z. Liu, Correlations for boiling heat transfer characteristics of high-velocity circular jet impingement on the nana-characteristic stagnation zone., International Journal of Heat and Mass Transfer, 72 (2014) 177-185.
[20] F.L. Cui, F.J. Hong, P. Cheng, Comparison of normal and distributed jet array impingement boiling of HFE-7000 on smooth and pin-fin surfaces, International Journal of Heat and Mass Transfer, 126 (2018) 1287-1298.
[21] S. Narumanchi, A. Troshko, D. Bharathan, V. Hassani, Numerical simulations of nucleate boiling in impinging jets: Applications in power electronics cooling, International Journal of Heat and Mass Transfer, 51(1-2) (2008) 1-12.
[22] S. Abishek, R. Narayanaswamy, V. Narayanan, Effect of heater size and Reynolds number on the partitioning of surface heat flux in subcooled jet impingement boiling, International Journal of Heat and Mass Transfer, 59 (2013) 247-261.
[23] L. Qiu, S. Dubey, F.H. Choo, F. Duan, Effect of conjugation on jet impingement boiling heat transfer, Internation Journal of Heat and Mass Transfer, 91(0017-9310) (2015) 584-593.
[24] K. Esmailpour, A. Azizi, S.M. Hosseinalipour, Numerical study of jet impingement subcooled boiling on superheated surfaces, Scientia Iranica, 26(4) (2019) 2369-2381.
[25] V.S. Devahdhanush, I. Mudawar, Critical heat flux of confined round single jet and jet array impingement boiling, International Journal of Heat and Mass Transfer, 169(0017-9310) (2021).
[26] ANSYS Fluent Theory Guide, in: Release 21.1, 2021.

[27] W.E. Ranz, W.R. Marshall, Evaporation from drops, Part 1, Chemical Engineering Progress, 48(3) (1952) 141-146.
[28] A. Tomiyama, Struggle with computational bubble dynamics, in: Third International Conference on Multiphase Flow, Lyon, France, June 8-12, 1998.
[29] M. Ishii, Two-fluid model for two-phase flow, in: 2nd international workshop on two-phase flow fundamentals, RPI, Troy, NY., 1979.
[30] T. Frank, J.M. Shi, A.D. Burns, Validation of Eulerian multiphase flow models for nuclear safety applications, in: Third International Symposium on Two-Phase Flow Modeling and Experimentation, Pisa,Italy., 2004.
[31] S.P. Antal, R.T. Lahey, J.E. Flaherty, Analysis of phase distribution in fully developed laminar bubbly two-phase flow, International Journal of Multiphase Flow, 17(5) (1991) 635-652.
[32] M.L.d. Bertodano, Turbulent bubbly flow in a triangular duct, in, Rensselaer Polytechnic Institute, New York, 1991.
[33] A.A. Troshko, Y.A. Hassan, A two-equation turbulence model of turbulent bubbly flow, International Journal of Multiphase Flow, 22(11) (2001) 1965-2000.
[34] N. Kurul, M.Z. Podowski, On the modeling of multidimensional effects in boiling channels, in: Proceedings of the 27th National Heat Transfer Conference, Minneapolis, Minnesota, USA, 1991.
[35] Y. Egorov, F. Menter, Experimental implementation of the RPI wall boiling model in CFX-5.6, in, Technical Report ANSYS/TR-04-10, ANSYS GmbH, 2004.
[36] V.H. Del Valle, D.B.R. Kenning, Subcooled flow boiling at high heat flux, International Journal of Heat and Mass Transfer, 28(10) (1985) 1907-1920.
[37] R. Cole, A photographic study of pool boiling in the region of the critical heat flux, AlChE Journal, 6 (1960) 533-542.
[38] M. Lemmert, L.M. Chawla, Influence of flow velocity on surface boiling heat transfer coefficient in Heat Transfer in Boiling. E. Hahne and U. Grigull, Eds., Academic Press and Hemisphere,New York, NY, USA, 1977.
[39] H.C. Unal, Maximum bubble diameter, maximum bubble growth time and bubble growth rate during subcooled nucleate flow boiling of water up to 17.7 MN/m^2, International Journal of heat and Mass Transfer, 19 (1976) 643-649.
[40] F.J. Moraga, R.T. Bonetto, R.T. Lahey, Lateral forces on spheres in turbulent uniform shear, International Journal of Multiphase Flow, 25 (1999) 1321-1372.
[41] I.H. Bell, J. Wronski, S. Quoilin, V. Lemort, Pure and pseudo-pure fluid thermophysical property evaluation and the open-source thermophysical property library CoolProp, Industrial & Engineering Chemistry Research, 53(6) (2014) 2498-2508.

Appendix A

The data for Fig. 17 and Fig. 19 are summarised in tables A-1 and A-2, respectively.

Table A-1: Fig. 17 Data

H/D	Re	HTC_{Total}	$HTC_{Quenching}$	$HTC_{Evaporation}$
1	10000	27.51	4.76	22.75
	15000	31.41	10.64	20.76
	20000	33.82	16.53	17.29
2	10000	29.14	5.32	23.82
	15000	30.71	9.97	20.74
	20000	32.84	15.40	17.44
3	10000	28.80	5.57	23.22
	15000	31.59	10.96	20.64
	20000	32.69	15.13	17.56
4	10000	30.93	7.11	23.82
	15000	31.39	10.31	21.08

	20000	31.39	10.31	21.08

Table A-2: Fig. 19 Data

H/D	Re	HTC_{Total}	$HTC_{Quenching}$	$HTC_{Evaporation}$
1	30000	32.25	2.79	29.47
	40000	32.07	3.19	28.89
	50000	31.90	3.47	28.43
2	30000	34.51	3.01	31.50
	40000	33.54	3.44	30.10
	50000	32.77	3.69	29.08
3	30000	37.48	2.85	34.63
	40000	35.38	3.34	32.04
	50000	34.12	3.62	30.50
4	30000	40.19	2.40	37.79
	40000	37.95	2.91	35.04
	50000	36.03	3.31	32.72